Electrocorticographic Features and Classification of Intracranial Glioma

by

Benjamin Lambert

A thesis

presented to the University of Waterloo

in fulfillment of the

thesis requirement for the degree of

Master of Applied Science

in

Systems Design Engineering

Waterloo, Ontario, Canada, 2021

Author's Declaration

This thesis consists of material all of which I authored or co-authored: see Statement of Contributions included in the thesis. This is a true copy of the thesis, including any required final revisions, as accepted by my examiners.

I understand that my thesis may be made electronically available to the public.

Statement of Contributions

The publications that resulted from the work presented in this thesis:

A. Diana C. Ghinda, **Benjamin Lambert**, Junfeng Lu, Ning Jiang, Eve Tsai, Adam Sachs, Jin-Song Wu, and Georg Northoff "Scale-free analysis of intraoperative ECoG during awake craniotomy for glioma" (published journal article - Frontiers in Oncology)

Abstract

During surgical resection of tumorous intracranial tissue in the human brain, different methods are used to locate the boundaries of the tumorous tissue because maximal resection of the tumorous tissue has been associated with better post-surgical outcomes for patients [1]. Electrocorticography (ECoG) is one method used intraoperatively to classify tissue as tumorous or healthy tissue. The electrophysiological features of neural tissue in the presence of tumorous intracranial tissue remain relatively unexplored. The exploration of these electrophysiological features may lead to more accurately defined tumorous tissue boundaries and improved post-operative outcomes. In this thesis study the Power Law Exponent (PLE) is explored as a feature for use in the classification of tumorous tissue. Spectral amplitudes and functional connectivity features are also explored as features for use in the classification of tumorous tissue. Three different classifier types, discriminant analysis, support vector machines (SVMs), and artificial neural networks (ANNs), are used with the features explored in this paper to study the relative values of the features for use in the generalized classification of tumorous tissue. ECoG datasets from 17 subjects were selected from a pool of 23 awake, resting state datasets belonging to subjects with WHO grade II-IV intracranial glioma. ECoG electrodes labelled "healthy" or "tumorous" were studied using PLE, spectral amplitude, and functional connectivity features and it was found that the PLE feature was the most valuable in the classification of tumorous tissue. The largest significant difference between the mean values of the distributions of healthy and tumorous tissue was found in the case of the PLE feature ($\mu_{healthy} = 3.676, {\sigma^2}_{healthy} = 0.178$, $\mu_{tumorous} = 3.214$, ${\sigma^2}_{tumorous}$ $p = 6.224\text{x}10^{-20}$). A three-layer Multi-Layer Perceptron (MLP) ANN was firstly trained on all features and secondly trained on all features without the PLE. The model trained with all features achieved a correct classification rate of 79.3% while the model trained without PLE achieved a correct classification rate of 62.7%.

Acknowledgements

I would like to express my sincere gratitude to my supervising Professor Ning Jiang for his limitless patience and direction, and his generous financial support during my work on this project and thesis. This project could not have been completed without his insight at critical points of the study and his expert management of my timely production of this work went above and beyond the expectations of everyone who supported me during my MASc program. I have experienced second-hand the difficulty in producing MASc research without the direction of a supervisor and I cherish the fact that I have been lucky to experience the absolute best of supervising professorship under Ning Jiang.

I would like to extend sincere thanks to Dr. Diana Ghinda for leading the production of the accepted manuscript produced for the work completed during this thesis project, and for the time and effort that went into the procedures performed necessary for the collection of the data used in this project. I would also like to thank her for the impressive amount of time she was able to spare working with me collaboratively to produce a manuscript while she was seeing patients at Johns Hopkins.

Special thanks to Prof. Jinsong Wu whose extraordinary knowledge, skills and unconditional support made this work possible. Also, many thanks to the entire glioma surgery team including Drs. Junfeng Lu, Zhang Jie, Zhong Yang, Jian-Bing Shi and Zhengda Yu for their assistance with data collection.

I would like to thank Lin Yao for taking the time to introduce me to this project and to Georg Northoff. I would like to thank Georg Northoff for giving me the opportunity to continue working on this project with the brilliant Diana Ghinda.

I would like to thank Sarah Pearce, Eric Lloyd, Aravind Ravi, and Mei Lin Chen for the help they unknowingly provided me during the writing phase of my thesis. I referred to their theses on UWSpace for formatting and structure directions.

I would like to thank my parents and my brother and his partner for their support and understanding sharing the same living space with me during the time I worked to produce this thesis.

Table of Contents

List of Figures

List of Tables

List of Abbreviations

ANN – Artificial Neural Network

CAR – Common Average Reference

CGSA - Coarse-Graining Spectral Analysis

ECOG - Electrocorticography

EEG – Electroencephalography

KS – Kolmogorov-Smirnov

LAC - Linear Amplitude Coupling

LDA – Linear Discriminant Analysis

MLP – Multi-Layer Perceptron

MRI – Magnetic Resonance Imaging

MSC – Magnitude Squared Coherence

PLE - Power Law Exponent

PLI - Phase Lag Index

PLV – Phase Locking Value

PSD – Power Spectral Density

QDA – Quadratic Discriminant Analysis

SVM – Support Vector Machine

1. Introduction

During surgical resection of tumorous intracranial tissue in the human brain, different methods are used to locate the boundaries of the tumorous tissue; maximal resection of the tumorous tissue has been associated with better post-surgical outcomes for patients [1]. Conventionally, functional magnetic resonance imaging (fMRI) is used to identify the existence, and to define the boundary, of structural lesions such as tumorous tissue. Electrocorticographic (Electrocorticography: ECoG) evidence, in supplement, is required to associate the lesion with epileptic activity. ECoG can also be used to define the tumour boundary intraoperatively, and the electrophysiological features of neural tissue in the presence of tumorous intracranial tissue remain relatively unexplored. The exploration of these electrophysiological features may lead to more accurately defined tumorous tissue boundaries and improved post-operative outcomes.

For ECoG data from awake and resting subjects, there are three objectives of this thesis study:

1. Evaluate the utility of the power law exponent (PLE) in the classification of tumorous tissue;
2. Evaluate the utility of functional connectivity features and spectral amplitude features in the classification of tumorous tissue;
3. Classify tumorous tissue using PLE, functional connectivity features, and spectral amplitude features and determine which features are more important for achieving high classification performance for tumorous tissue.

2. Literature Review

2.1 Intracranial Glioma

Glioblastomas are the most common primary malignant brain tumours and are associated with large repercussions on cognitive function and poor life expectancy. The World Health Organization classifies gliomas into four histological grades: I, II, III, and IV, where the lower grade tumours progress to become higher grade tumors over time [1]. Diffuse low-grade gliomas are highly epileptogenic brain tumours, meaning they are highly capable of causing an epileptic attack involving seizures, for example. Seizures are sudden, uncontrolled electrical disturbances in the brain that can cause a loss of control of behaviour, consciousness, and motor control [2]. While MRI is used to identify the existence of structural lesions such as glioma, Electroenecephalographic (Electroencephalography: EEG) evidence is required to associate the lesion with epileptic activity. EEG is a non-invasive measurement technique involving the placement of electrodes over the scalp for the measurement of electrical potentials produced by neural activity in the brain. EEG however, does not have enough spatial resolution to localize the epileptogenic area [3]. There is a growing body of evidence suggesting that greater surgical resection of the lesion as well as the epileptogenic zone results in improved overall survival, progression-free survival, and superior quality of life [4]. Electrocorticography (ECoG) has been used to locate the epileptogenic area for resection in patients with medically refractory localization related epilepsies [5]. ECoG is an invasive measurement technique involving the placement of electrodes directly on the exposed surface of the brain for the measurement of electrical potentials produced by neural activity in the brain. An illustration of an ECoG electrode grid used intraoperatively is shown below in Figure 3.

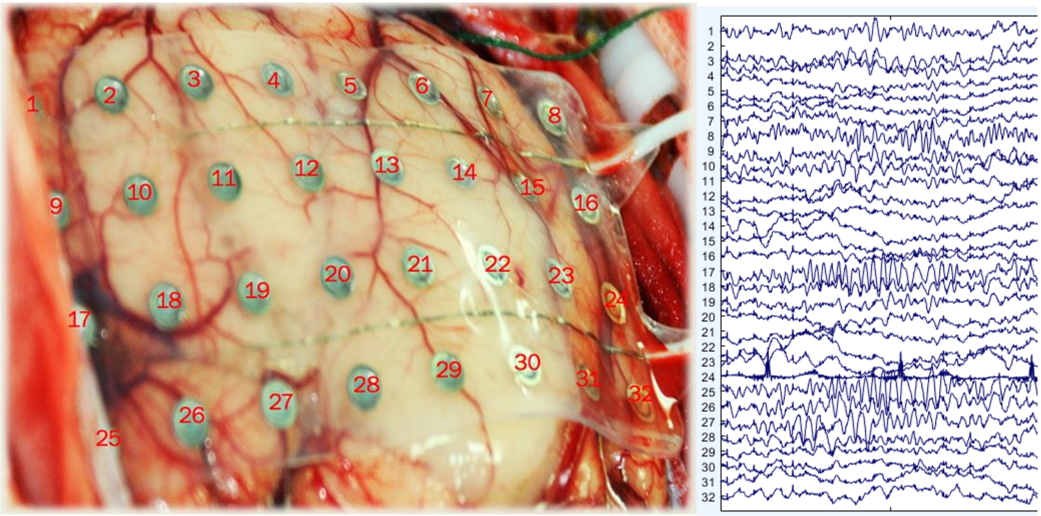

***Figure 1: Example ECoG Electrode Grid and Recorded Channel Data** [69].*
The electrode grid is shown on the left with superimposed electrode numerical identifiers. The measured electrical potentials of each electrode are shown in the right in arbitrary temporal and magnitude units.

2.2 Signal Properties and Processing of Electrocorticographical Data

In contrast to EEG, ECoG has a higher temporal (EEG: 10 ms, ECoG: 3 ms [6]) and spatial resolution (EEG: 5-9cm [7], ECoG: 1cm [6]) and less susceptibility to artifacts and noises [8]. The signal data measured for one EEG or ECoG electrode is referred to as a “channel”. ECoG electrodes commonly have diameter sizes of 2-3mm [9], and these electrodes have been understood to measure the aggregate electrical potential of neural activity on a large scale, each electrode measuring activity millimeters to centimeters from its location. Dubey et al. designed a hybrid ECoG, Local Field Potential (LFP), and Multi-Unit Activity (MUA) measurement device containing both microelectrodes to measure precise locations (LFP and MUA) and ECoG electrodes (2.3mm diameter) to pick up aggregate activity. They found that the spatial spread of electrical potentials, as measured with the ECoG electrodes, was local and not much larger than the size of the electrodes [9]. Dubey et al. also researched the spread of electrophysiological neural activity as a function of frequency and found that in the visual cortex of the macaque, the LFP spread in the frequency range of 60-150Hz was larger than for lower frequencies [10]. These frequencies are in a frequency spectral bandwidth called the Gamma bandwidth and they have been observed in a variety of functional brain systems, for example systems responsible for motor execution and planning, auditory processing, and visual-spatial attention [11]. Neuroelectrical signals, as measured using EEG or ECoG, are relatively contained within the bandwidth of 0-200Hz. Delta is the frequency range or bandwidth of 0-4Hz, theta is the 4-7Hz bandwidth, alpha is the 7-13Hz bandwidth, beta is the 14-30Hz bandwidth, and gamma is the 30-100Hz bandwidth. Digital signal processing is commonly used to retain or remove selected bandwidths from the ECoG data. Notch filters are often applied to the data to remove electrical power line noise sources, low pass filters are applied to remove the lowest spectral components to give the signals a stable baseline, and high pass filters are used to limit spectral content to the <200Hz bandwidth [12]. Spatial high-pass filtering is also commonly performed on ECoG data to reduce the degree to which signals from adjacent electrodes “leak” into an electrodes measured signal, a.k.a channel cross-talk. One of the most widely applied spatial filters in ECoG studies is the Common Average Reference (CAR) Filter for which a mean signal is calculated across all electrodes and subtracted from each electrode. The CAR can be computed as follows in Equation (1).

$$V_i^{CAR} = V_i^{ER} - \frac{1}{n}\sum_{j=1}^{n} V_j^{ER} \tag{1}$$

Where V_i^{ER} is the potential between the i^{th} electrode and the reference and n is the number of electrodes in the montage [13]. While this method reduces the ECoG signal variance that is not related to the signal being measured by one electrode, it can be seriously affected by single excessively noise channels prior to spatial filtering. The failure to remove single channels containing excessive noise can result in the CAR filter spreading that noise into other channels, *i.e.* spatial aliasing [14]. An alternative spatial filter to the CAR filter is the Laplacian spatial filter. This filter weights immediately or distantly spaced electrode signals equally and subtracts those weighted signals from a higher-weighted central channel. The Laplacian spatial filter can be computed as follows in Equation (2):

$$V_i^{LAP} = V_i^{ER} - \sum_{j \in Si}^{n} V_j^{ER} g_{ij} \tag{2}$$

where

$$g_{ij} = \frac{1}{d_{ij}} / \sum_{j \in Si}^{n} \frac{1}{d_{ij}} \tag{3}$$

Where Si is the set of surrounding electrodes of the ith electrode and d_{ij} is the distance between electrodes i and j (where j is a member of Si) [13]. This technique is designed well for applications in which the signals being measured by surrounding electrodes are also leaking into the electrode being recorded from [15]. Aside from noise removed within specific bandwidths, or common noise across all channels removed using a CAR filter, a temporally sporadic form of noise can exist in channel data as “artifacts”. These artifacts can come from muscular tissue and their production of electrical potentials, the electrical connections to the electrodes being physically moved, or other sources. EEG is particularly prone to artifacts created from ocular movements and blinking, jaw clenching, electrical interference from muscular tissue in the head, vibrations from walking or moving, etc, Comparatively, ECoG has been largely thought to be minimally affected by eye blink artifacts although Ball et al. demonstrated that these artifacts are present in the ECoG data to some extent [16]. Signal processing methods have been developed to remove specific components within ECoG time series data, for example Independent Component Analysis (ICA), which has been used to remove eye blink artifacts in EEG data [17].

2.3 Electrophysiological Features of ECoG

A variety of electrophysiological features of ECoG have been studied, some more widely than others, throughout literature. Spectral amplitude features are very well studied and are one of the quickest and easiest features to generate from the power spectral density estimates of time series data [12]. Wavelet features have also been well-studied and have been used to successfully classify healthy and tumorous neural tissue [18]. Functional connectivity describes the temporal correlations between spatially remote neurophysiological events and has been studied widely throughout literature in the form of Linear Amplitude Correlation (LAC), Magnitude Squared Coherence (MSC), Phase Lag Index (PLI), and Phase Locking Value (PLV) [19,20,21]. More advanced connectivity features are capable of accounting for directionality. These include Granger causality and the Directed Transfer Function [22]. The Power Law Exponent is a feature of log-log spectral data sampled from a power law distribution and is relatively unexplored in ECoG literature.

The PLE was chosen as the primary feature of interest for the work presented in this thesis due to it remaining relatively unexplored in ECoG literature. To compare the tumorous tissue classification performance using the PLE to classification performance using the most relevant features in literature, relative spectral amplitudes, LAC, MSC, PLI, and PLV were also chosen in this thesis work for further study.

2.3.1 Power-Law Scaling Behaviour

In the measurements of seismic activity, stock market fluctuations, and EEG, their power spectral densities are scaled according to a power law whereby lower frequencies have larger amplitudes and higher frequencies have smaller amplitudes [26]. The power law structure is approximately linear when plotted in a logarithmic-logarithmic frequency-amplitude plot. This power law scaling property is also called scale-free behaviour; no characteristic scales dominate the dynamics of the underling process. Examples of power-law scaling behaviour are shown below in Figure 2.

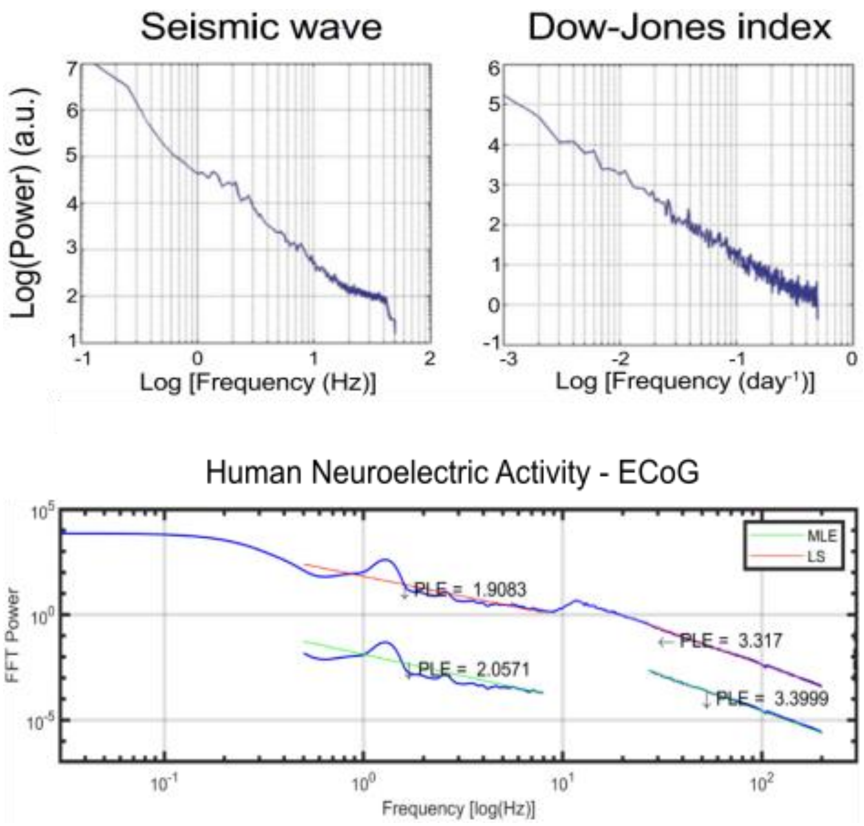

Figure 2:Examples of Power Law Scaling Behaviour. *[26]*
Seismic activity is shown on the top left, stock market fluctuations (specifically the Dow-Jones Index) is shown on the top right, and human neuroelectric activity is shown on the bottom for which example PLE estimates are given based on two different PLE algorithms (discussed further in the methods section).

In 1992 Pritchard et al. described power law scaling behaviour in the power spectral density of EEG and found that the degree of deviation such linearity was related to the power in the 8-12Hz bandwidth, usually referred as the alpha band [27]. Linkenkauer-Hansen et al. also found that EEG followed a power scale and that the amplitude fluctuations of 10 Hz and 20 Hz frequencies were correlation over thousands of oscillation cycles. These correlations were described as long-range temporal correlations (LRTCs) and it was found that the power law scaling exponents of EEG and MEG were the same [28]. Furthermore, it was found that large scale infra-slow (<1 Hz) oscillations 0.02 Hz to 0.2 Hz were correlated with the magnitude of higher frequency oscillations and also with epileptic events [29]. Additionally, the low frequency theta bandwidth (4-8 Hz) was found to modulate the power of the high gamma bandwidth neural activity (80-150 Hz) [30]. In 2019 Colombo et al. reported that the power law exponent (PLE) of the power spectral densities (PSDs) of EEG data discriminated states of consciousness from states of reduced consciousness (anesthesia) and that the PLE was also highly correlated to the perturbation complexity index (PCI) [24], which is an index that is known to measure conscious activity [31]. He et al. found widespread nested frequencies throughout the spectrum of human neural activity with lower frequencies modulating the amplitudes of higher frequencies. They also found that the PLE measured using functional magnetoresonance imaging (fMRI) was different from that of ECoG. The fMRI PLE was also found to be vary across brain regions [26]. Huang et al. found that the degree of the LRTCs, as indexed by the PLE, in spontaneous activity in the resting state, is related to the degree of the phase-dependent effect between spontaneous and evoked activity during a task [32]. The LRTCs between the activity of different bandwidths suggest that the characterization of a dataset using its power law characteristic could provide useful information for further studies. While Miller et al. measured power law scaling behaviour in the power spectral density estimate (PSD) of human ECoG recordings and showed that small scale simplified models of neurons could produce a power law structure, other researchers have proposed alternate sources of the structure. Bedard et al. measured LFPs in the cortex of cats and found that the power law scaling of neuronal activity did not rely on critical states and instead postulated that the power law scaling is created from electrical potentials being temporally filtered by extracellular material. They described how the extracellular media and neuronal membranes represent a complex network of electrical resistors and capacitors [33]. Almond et al. simulated the electrical noise in large networks of randomly positioned resistors and capacitors and found that the networks noise, measured at any point in the network, follows a power law [34]. Regardless of the cause of the PLE structure in human EEG and ECoG data, there is a considerable amount of support in literature for the utility of the PLE as a feature with which to associate different qualities of or patterns in neural activity. In the case of EEG and ECoG, power laws are typically fit on either side of the harmonic peaking alpha bandwidth of the PSD, representing lower frequency structure and higher frequency structure [35,36].

2.3.2 Spectral Amplitude Features

Activity in different spectral bands has been attributed to specific behavioural processes [23] and these spectral bands are widely used in literature as a metric for which to compare the effects of experimental procedures [12]. For example, theta rhythm oscillations occur in the 4-8 Hz bandwidth and larger amplitudes occur during drowsiness [24]. The amplitudes of spectral bands have been used successfully as a feature in a classifier for tumorous and healthy tissue. Boussen et al. found that there were significant decreases in the absolute power spectrum of tumorous tissue channels within the alpha, beta, and gamma spectral bands [25]. Band et al. also found that there was an overall power reduction across all frequency bands within tumorous tissue, compared to surrounding tissue [36].

2.3.3 Functional Connectivity and Related Algorithms

Functional connectivity describes the temporal correlations between spatially remote neurophysiological events while effective connectivity can be described as the influence one neuronal system exerts over another [19]. The linear correlation between channels, measured with the Pearson Correlation Coefficient, is the most widely used algorithm to measure functional connectivity [37]. Band et al. successfully used linear correlation to map the functional connectivity of intracranial glioma. They found that higher measurements of linear correlation between a channel and adjacent channels was constrained to regions of tumorous tissue [36]. Coherence, a generalization of correlation to the frequency domain, is sensitive to the effects of volume conduction. Volume conduction is the phenomenon by which signal sources underlying one measurement location can leak through neural and extracellular tissue to influence the signal measured at another spatial location. Due to volume conduction, in certain circumstances coherence may not measure the functional connectivity between different regions and instead measure the degree to which a signal source is present in different measurement locations. Nolte et al. propose the use of the imaginary component of complex coherency to measure the interaction between channels as phase dependence [20]. Multiple methods of measuring phase dependence have been applied successfully in the study of intracranial glioma. Two such methods are the phase locking value (PLV) and the phase lag index (PLI)

[25]. The PLI is based on the theory that the existence of non-zero phase lag between two time series cannot be explained by volume conduction from a single source, and it is measured as a statistic over a defined time window of how many samples are leading or lagging between the time series [38]. The PLV is similar to the PLI, as both use the Hilbert Transform to obtain the instantaneous phase of a time series [21]. The PLV compares the difference between the instantaneous phases of two time series, representing the phase differences in complex form and averaging them across trials to arrive at a mean complex representation of phase difference. If the magnitude of the complex representation is large, it implies that the distribution of phase differences had a smaller variance around a mean value and thus the time series are more phase-locked together. If the magnitude of the complex representation is small, it implies that the variance of the phase differences is large around a mean value and thus there is a lower amount of phase locking between time series [39]. Boussen et al. used both the PLI and the PLV to classify intracranial cortical tumorous tissue and found that the PLI and PLV both measured significant differences between tumorous and healthy tissue [25].

2.4 Classifiers and Performance In Literature

Classifiers predict the class of a given set of data points, mapping a set of input variables to a discrete set of output variables. Classifiers can be trained to predict whether some sample of data is a measurement from tumorous intracranial tissue or not. Different classification methods have been applied to the problem of tumorous tissue classification, including linear discriminant analysis (LDA), support vector machines (SVM), and artificial neural networks (ANN) [18,25,40,41,42,43]. These three classification methods were applied in the work presented here and the results are discussed, comparing their performances against each other. Discriminant analysis is the process of training some discriminant function such that a decision boundary is created between the datasets of two different classes. The variables used to train and test the discriminant function are known as features. New feature samples input to the discriminant function result in an output from the function that “classifies” the samples as one class or another. In the case of tumorous tissue the classes would be “healthy”, “peritumoral”, and “tumorous”. The assumptions that are made in the application of discriminant analysis are that the class conditional densities are approximately normal and that the sampled features are good estimates of the population features [44]. Velilla et al. found that it is the elliptical symmetry and not normality of classifier inputs that is the key aspect for correct performance. When class probabilities are identical and sample size is large enough, it was found that performance is not related to the gaussian assumptions of the conditional probabilities of the classes [45]. Support Vector Machines (SVM) were originally created by Vapnik and Cortes as a potential alternative to artificial neural networks as classifiers [46]. The SVM method finds a hyperplane lying between two classes. The optimal hyperplane lies orthogonal to the optimal margin between classes. Data points lying directly on the margin edge are called the support vectors [46]. Different kernel functions are used to map an input feature space nonlinearly into a higher dimensional feature space where a hyperplane can be created between two classes with maximum margin. [47]. SVMs can be applied to multiclass problems but its original implementation was designed for binary scenarios [48]. Artificial Neural Networks are data driven self-adaptive methods in that they can adjust themselves to the data without any explicit specification of functional or distributional form for the underlying model [49]. Multi-layer perceptrons (MLPs) are a type of ANN with one or more layers of nodes between input and output nodes. The single node computes a weighted sum of its inputs, subtracts a threshold, and passes the result to a non-linearity, producing a binary output decision. A three-layer perceptron can form arbitrarily complex decision regions and can form regions as complex as in mixture distributions or nearest-neighbour classifiers [50].

In literature, multiple studies reported the performance of classifiers applied to the problem of classifying intracranial tumorous tissue. Karameh et al. studied the EEG data of 9intracranial glioma patients and used frequency and wavelet features with multi-layer self-organizing maps to achieve a channel-wise correct classification rate of nominally 90%[40]. Murugesan et al. used EEG to study the classification of tumorous tissue using SVM and ANN classifiers, achieving a correct classification rate for tumorous channels of 98.8% using a multilayer perceptron model with one hidden layer [41,42]. Selvam et al. studied 3 healthy subjects and 6 intracranial glioma subjects and achieved a correct classification rate of 91.8% for tumorous tissue using a modified wavelet-independent component analysis technique and a three-layer MLP with EEG data [43]. Sharanreddy et al. also used wavelet analysis techniques for feature extraction in the EEG data of 25 subjects with intracranial glioma and achieved a correct classification rate of 87% for tumorous tissue using a MLP with one hidden layer [18]. Lastly, Boussen et al. used spectral amplitudes and functional connectivity features (including linear correlation, magnitude squared coherence, PLI, and PLV) to extract features from the ECoG data of 16 of 25 total patients with intracranial glioma and achieved a correct classification rate of 87% using a two-layer feed forward network with a sigmoid transfer function in the 15-neuron hidden layer and a softmax transfer function in the two-neuron output layer [25]. While correct classification rates are high in literature, sample sizes are not consistently large enough and the pr-processing and data exclusion criteria are not always discussed in thorough detail. For these reasons, the reproducibility of the research is called into question. This reproducibility must be explored further by confirming classifier performance across different datasets.

3. Methods

3.1 Subjects, Systems, and Procedures

Twenty-three patients with a newly diagnosed intracranial glioma, out of which six presenting with multiple seizures were enrolled. The patients' demographics including the presenting symptoms are presented in Table 1 below.

Table 1: Subject Demographics and Relevant Diagnoses

Subject	**Age**	**Sex**	**Tumor Location**	**WHO Grade**	**Presenting Symptoms**
1	43	M	Temporal	II	Generalized seizure, motor – tonic-clonic
2	34	F	Frontal	IV	Generalized seizure, motor – tonic-clonic
3	50	F	Frontal	III	Focal aware seizure, non-motor onset-sensory
4	40	M	Frontal & insular	III	Focal aware seizure, motor onset-epileptic spasm
5	39	M	Temporal & insular	IV	Focal aware seizure, non-motor onset-autonomic
6	31	F	Frontal	II	Generalized seizure, motor – tonic-clonic
7	46	F	Fronto-temporal	II	Focal aware seizure, motor onset-epileptic spasm
8	34	M	Fronto-temporal	II	Generalized seizure, motor – tonic-clonic
9	29	F	Parietal	II	Generalized seizure, motor – tonic-clonic
10	64	M	Temporal	IV	Contralateral sensory changes
11	52	F	Frontal	IV	Contralateral weakness
12	72	M	Frontal	IV	Generalized seizure, motor – tonic-clonic; contralateral weakness
13	35	F	Frontal	II	Generalized seizure, motor – tonic-clonic
14	38	M	Frontal - parietal	II	Contralateral sensory changes
15	49	F	Frontal	III	Focal aware seizure, non-motor onset-sensory
16	49	F	Frontal	II	Incidental
17	42	M	Frontal	II	Incidental
18	35	M	Fronto-temporal	IV	Contralateral weakness, aphasia
19	13	M	Parietal	I	Generalized seizure, motor – tonic-clonic
20	41	F	Frontal & parietal	II	Headaches
21	34	M	Frontal	II	Generalized seizure, motor – tonic-clonic
22	33	F	Frontal	II	Contralateral sensory changes
23	41	F	Frontal	II	Headaches

All patients underwent awake craniotomy for tumor resection. A monitored anesthesia care approach was adopted for all patients as per previous publications [51]. After the anesthesiologists administered premedication by infusing 0.02–0.03 mg/kg midazolam and 5 mg tropisetron, intravenous lines, a central venous catheter, an arterial line, and a urethral catheter were inserted. The supraorbital, supratrochlear, zygomaticotemporal, auriculotemporal, greater occipital, and lesser occipital nerves were blocked bilaterally using a mixture of lidocaine (0.67%) and ropivacaine (0.5%). Once the patient was brought into moderate sedation with boluses of intravenous propofol, the head was fixed into its fitted position using a custom-designed high-field MRI-safe head holder (DORO Radiolucent Headrest System, Pro Med Instruments GmbH, Freiburg, Germany), which was integrated with an intraoperative MR imaging system (IMRIS™) . Once the scalp was prepared and draped, remifentanil (0.01–0.03 lg/Kg/min) or dexmedetomidine (0.1–0.7 lg/Kg/h) were administered for analgesia. To minimize brain welling, mannitol (1 g/kg) was infused intravenously before the dura opening. Because of the minimal draping used, no laryngeal mask airway or endotracheal tubing was applied. The ECoG grid was placed over the exposed brain surface as indicated by the needs of the patient. ECoG signals were recorded with a 20, 32 or 48-channel grid of 4.0 mm diameter electrodes with 2.3mm exposure (Ad-tech, Germany) connected to a BP amplifier (Brain Product, Germany). The reference electrode was placed on the contralateral earlobe to avoid any potential increase in coherence due to the reference electrode location. 5 min of recording in the awake state were acquired prior to the tumor resection. For the six patients presenting with seizures, the ECoG signal was also acquired in the anesthetic state. The signals were sampled at 2500 Hz.

3.2 Tissue Labelling

The ECoG electrodes for each patient were classified in TT (tumoral tissue), HT (macroscopically healthy-tissue) and PT (peritumoral tissue) according to the radiological defined boundaries as per the conventional structural MRI. An intra-operative picture was taken after the electrode grid was placed over the exposed brain. Intra-operative location of each electrode were recorded with the neuro-navigation system (Medtronic, Inc., Minneapolis, MN, USA). Image guided localisation of the electrode location were performed as soon as possible after the craniotomy was completed in order to minimize potential brain shift. The electrode location was recorded using the intra-operative Medtronic neuronavigation system. The accuracy of the neuronavigation approach used is well established and represents the standard method for image-guided resection of brain tumors [52,53]. The electrodes were classified as overlying the tumoral, peritumoral or macroscopically healthy tissue. This was performed for each patient according to the radiological defined boundaries as per the conventional structural MRI: FLAIR for non-enhancing diffuse low-grade gliomas and the T1 MPRAGE with contrast for contrast enhancing tumors [54]. The peritumoral tissue was defined as an area within a two cm margin from tumor borders according to the RANO criteria [55]. All MR brain images were acquired one or two days preoperatively in the diagnostic room of an iMRI-integrated neurosurgical suite using a 3T Siemens MRI scanner (Siemens MAGNETOM Verio 3.0 T, Germany) with a standard 32-channel head coil. The cortical surface was segmented from the pre- operative MRI using the Analysis of Functional NeuroImages software (http://afni.nimh.nih.gov/afni). Intra-operative photograph was superposed on the segmented cortical surface in order to confirm the electrode location in respect to the tumor with the help of visible sulcal patterns on the cortical surface obtained from the pre-op.

3.3 Pre-processing of ECoG Data

The ECoG data of all subjects for the Awake Rest state was pre-processed prior to further analysis. Pre-processing methods applied to the data include down-sampling, temporal filtering, and spatial filtering. Poor-quality ECoG channels were removed from the dataset prior to spatial filtering. No artifact removal methods were applied prior to the preprocessing methods mentioned above, as it was expected that the ECoG signal quality would be unaffected by artifacts such as eye-blinking, facial muscle electrical activity, or other sources. There is some evidence to suggest the contrary however, such as in the work of Tonio Ball et al, who studied the presence of eye blinking related electrical activity in ECoG recordings [16]. These artifacts will be evaluated and removed in additional studies with this data.

3.3.1 Temporal and Spatial Filtering

Temporal filters were initially applied to the data. All filters applied in this stage were Hamming windowed sinc FIR filters created through the EEGLAB ‘pop_eegfiltnew’ function in MATLAB. All brain activity of interest was determined to belong to the 1-190Hz frequency range, as human neuroelectric signals are relatively contained within this bandwidth [12] and activity around 200Hz contains harmonics from power line interference. The data was low-pass filtered with a cut-off frequency of 190 Hz and then downsampled from 2500 Hz to 1000 Hz to reduce signal processing time while assuring that the 1-190 Hz bandwidth is sampled accurately. The MATLAB function ‘resample’ was used for this decimation. Stop-band filters with a 10 Hz stopband were applied at 50Hz, 100Hz, and 150Hz locations to mitigate the effect of power line interference and its aliases. Lastly, a high-pass filter was applied with a cut-off frequency of 1 Hz to remove the effect of very low frequency drift from the ECoG measurements.

A common average reference (CAR) filter was applied after temporal filtering to remove common source noise. CAR filters have been shown to reduce ECoG signal variance that is not related to the neural activity being measured [14]. CAR filters can introduce channel specific noise to all channels if proper channel and artifact removal methods are not applied to the data before applying the filter. Manual channel removal was done prior to CAR filter application however, so this should not be of concern for the work presented here.

3.3.2 Channel Removal Method

Following the application of temporal filters, all ECoG data channels for each subject were visually reviewed, by an experienced human evaluator, for quality before application of the CAR filter. The MATLAB toolbox EEGLAB was used to visualize the ECoG data for all subjects. ECoG channel data was deemed to be poor quality if, for the majority of the temporal length of data and relative to other channels, there was an excessively large low frequency amplitude or baseline wander, channel data had a near constant value (flatlined), had noticeably excessive high frequency content, or there were too many channels containing nearly identical data (electrical shorting between electrodes). Poor quality channels were then removed from the dataset of each subject and if any subjects had five or more poor quality channels, those subjects were excluded from the study. The reasoning for excluding subjects is that if subjects have too many poor quality channels, this is evidence of systematic error being introduced to the measurement system and thus there could be some biasing effect remaining within the higher quality channels from that same subject. Exclusion in this case is a conservative control of systematic error. Table 2 below documents which channels and subjects were removed from further analysis.

Table 2: Poor Quality Channels and Exclusion List

Subject	Total Channels	Poor Quality Channels	Excluded Subject [x]	Reason For Exclusion
6	32	All	x	Excessive high frequency noise
9	32	2,3,4,5,7,27,28		
10	32	4,7,8,16,24,32		
14	32	All	x	Too many channels identical (short)
19	32	5,9,10,22,24,25,30,31		
20	32	5,10,15,20,23,24,26,27,32		
22	32	16,24,31		
29	32	21-32	x	Flatlined channels
35	32	19-31	x	Flatlined channels
36	32	All	x	Dataset corrupted
38	32	24		
40	32	24,29,30,31,32		
41	32	10,16,25		
43	32	8,16,24,32		
44	32	16,24,32		
48	32	7,8,15,16,22,23,24,30,31,32		
52	32	4,8,16,18,24		
53	32	4,5,6,24		
54	32	8,16,24,27,32		
55	32	8,16,24,25,26		
57	32	2,24		
60	32	All	x	Too many channels identical (short)
65	32	24,25,26		

Following the exclusion of channels and subjects from further study, feature extraction methods were applied to the dataset to collect features with which to classify glioma tissue, tissue bordering glioma (peritumoral tissue), and healthy neural tissue.

3.4 Feature Extraction

Features were extracted from the dataset to represent specific electrophysiological properties of neural activity. These features include the Power Law Exponent (PLE) and relative spectral amplitudes, which measure properties of the spectral structure of a time series of ECoG data, and four features that measure the functional connectivity between ECoG electrodes: the Phase Lag Index (PLI), Phase Locking Value (PLV), Magnitude-Squared Coherence (MSC), Linear Amplitude Correlation (LAC).

3.4.1 The Power Law Exponent

The Power Law Exponent (PLE) is a feature of a time series of data for which its power spectral density (PSD) is well-fit by a power law. A quantity x is defined by a power law if it is sampled from a probability distribution

$$p(x) \propto x^{-\alpha}, \tag{4}$$

where α is the scaling parameter of the distribution known as the scaling parameter or exponent. Two different methods of deriving this power law exponent were applied to the ECoG data. With the first method, widely used throughout ECoG PSD literature [24,26,27,29,30,32,33], a least-squares linear regression was performed on the logarithm of the histogram of spectral samples or PSD. With the second method, a maximum likelihood estimator of the PLE was derived and applied to the logarithm of the PSD. This second method represents a proposed, improved alternative to the first method which is prone to larger systematic error resulting from applying linear regression to a logarithmic independent variable [56]. To determine whether a power law was a good fit to the PSD of the ECoG data, the Kolmogorov-Smirnov Test (KS test) was applied and the goodness of fit of each of the two PLE derivation methods were compared to each other.

Prior to the calculation of PLE for each ECoG channel of each subject, Coarse-Graining Spectral Analysis was applied to the data to reduce the amplitude of oscillatory harmonic activity which can bias the PLE estimation.

3.4.1.1 Coarse-Graining Spectral Analysis

Coarse-Graining Spectral Analysis is an algorithm designed to separate harmonic spectral activity from non-harmonic, scale-free spectral activity [57]. For time series data of interest, a duplicate time series is made by sampling that time series at a more coarse interval, for example, sampling every other point. The cross-power spectra of these two time series will theoretically preserve any scale free components while diminishing the harmonic components due to the fact that the statistical distribution of the scale-free components will remain the same when sampled at different rates [58]. Yoshiharu Yamamoto and Richard L. Hughson first published this method as a tool to be used for studying heart rate variability [59] but it has been applied by He et al. to remove harmonic activity prior to measuring ECoG PLE [26]. As in the work of Yamamoto and Hughson, rather than creating a second times series by sampling the first series at a different rate, an alternative approach was taken whereby channel time series were split into two copies. The epochs of these copies were arranged in two different ways and the cross-power spectra generated with the two different arrangements. In Yamamoto and Hughson 1991 [59], ECG data was separated into a series of epochs based on R-R intervals. The first time series was represented by the original series of epochs. The second series was created by duplicating every other epoch so that the total number of epochs in each series was the same, thus allowing for the cross-power spectra to be created in a straightforward way. In the work presented here, a series of 40-second epochs with 50% overlap were created for each channel, two separate series of smaller epochs, 20-seconds in length, were created from this original epoch series. For Epoch Series 1, the 20-second epochs were sampled from the beginning of the 40-second epochs while for Epoch Series 2, the 20-second epochs were sampled from the end of the 40-second epochs. As sampling was iterated from the original 40-second Epoch 1 through Epoch ‘n’, where n is the number of epochs in the 40-second epoch series, a time shift was employed such that for Epoch Series 1 the 20-second epoch was sampled $t = \frac{20}{n}$ seconds forward from where it was sampled in the previous 40-second epoch. For Epoch Series 2, the 20-second epoch was sampled $t = \frac{20}{n}$ backwards from where it was sampled in the previous 40-second Epoch. This process is shown below in Figure 4.

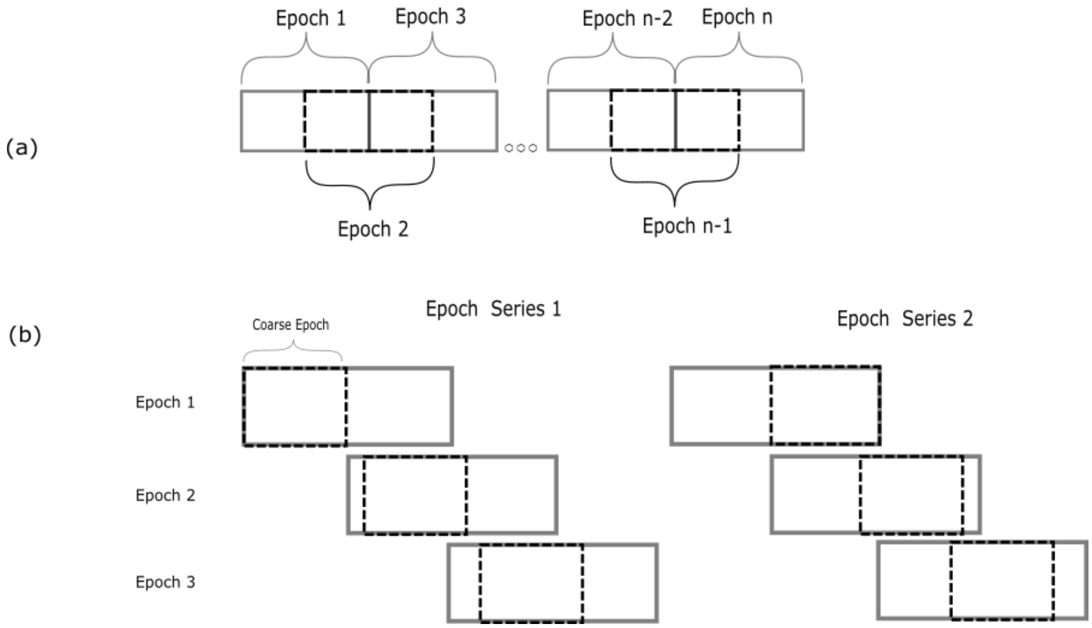

Figure 4: Coarse-Graining Spectral Analysis Epoch Series Design

The cross-power spectra between Epoch Series 1 and Epoch Series 2 were then generated using the 'cpsd' function in MATLAB which create a cross power spectral density estimate using Welch's averaged, modified periodogram method of spectral estimation. A single mean spectral estimate was created by averaging over the series of resulting cross power spectral densities. This final mean spectrum is a spectral estimate that contains less harmonic activity than an auto power spectral density estimate created from only Epoch Series 1 or Epoch Series 2.

In the spectral estimates created from this method it was noted that the harmonic activity that CGSA was designed to reduce was still apparent, appearing only slightly reduced than for the auto power spectral estimates. It should be noted here that this method is founded with the assumption that two different sampling methods should measure harmonic activity differently but not scale-free activity. This assumption becomes more false as harmonic activity becomes more present at the same scale throughout the data. In the case that harmonic activity is present at a single scale throughout the entire temporal length of the data, there is no coarse graining sampling scheme that can remove the harmonic activity using CGSA. He et al. 2010 found that, following their application of CGSA to ECoG time series, the “shoulder” of harmonic activity they were trying to remove in the spectral estimate was not as reduced in magnitude as they had hoped [26]. For future applications of CGSA, the presence of undesired harmonic activity should be used as a temporally dependent variable according to which coarse-grained epochs should be selected from.

3.4.1.2 PLE – Least Squares Linear Regression Estimate

Following application of CGSA to filtered, high-quality ECoG channels, a harmonic-reduced, averaged PSD estimate is obtained. Due to the application of band-stop filters for the 45-55Hz, 95-105Hz, and 145-155Hz spectral bands, these bands in the PSD are highly attenuated. To achieve a more continuous PSD structure for PLE estimation, a linear interpolation was used to overwrite the data in these bands. The averaged spectral amplitudes in 1Hz bands immediately prior to and following each band were used as interpolation endpoints. This method will introduce some bias into the PLE estimation due to simulated data being added to the sampled data PSD. By using simulated data through the band-stop bandwidths, a single PLE for higher frequency content could be generated across a larger number of samples which decreased the amount of systematic error in the PLE estimation. This trade-off was assumed to be acceptable, although future works should compare the likely amount of error introduced to the estimate with this approach.

Two PLEs were estimated for one PSD: a “pre-alpha PLE” was estimated in the 0.5-8Hz band, and a “post-alpha PLE” was estimated for the 27-190Hz band. All ECoG channel PSDs contained a “knee” in the bandwidth containing alpha and beta wave content (nominally 8-27 Hz), which would have significantly biased PLE estimates made through this band. Other studies have also made the decision to estimate the PLE outside the alpha/beta bands for similar reasons [36,60]. The logarithm of the spectral frequencies and the associated spectral amplitudes for the pre-alpha and post-alpha bands were then input into the MATLAB ‘fit’ function. The slope of the regression line fit to the log-transformed data was then extracted as the PLE. This method is henceforth referred to as the “LS” method.

3.4.1.3 PLE – Maximum Likelihood Estimate

The maximum likelihood estimate (MLE) of the PLE avoids the bias error introduced to the PLE calculation with linear regression whereby the assumption of normally distributed error is broken due to the logarithm transformation of the amplitude and frequency dimensions prior to curve-fitting [56]. The MLE PLE was applied to the CGSA-processed PSD, stop-band interpolation was applied, and PLE estimates generated for both pre-alpha and post-alpha PLE. The MLE PLE provides accurate parameter estimates in the limit of large sample size [56]. For this reason, the post-alpha bandwidth is more accurately represented, as there is a lesser number of PSD data points in the pre-alpha 0.5-8Hz bandwidth. The continuous power law distribution is given as

$$p(x) = \frac{\alpha - 1}{x_{min}} \left(\frac{x}{x_{min}} \right)^{-\alpha}, \tag{5}$$

where α is the PLE and x_{min} is the minimum value at which power-law behaviour holds. x_{min} was chosen in avoidance of the knee of the PSD described previously, spanning the 8-27Hz bandwidth. For the pre-alpha PLE $x_{min} = 0.5Hz$ and for the post-alpha PLE $x_{min} = 27Hz$. Given a dataset containing n observations $x_i \geq x_{min}$, the likelihood of the data given the power law model becomes [56]

$$p(x \mid \alpha) = \prod_{i=1}^{n} \frac{\alpha - 1}{x_{min}} \left(\frac{x_i}{x_{min}} \right)^{-\alpha}. \tag{6}$$

The MLE PLE is then derived to be

$$\hat{\alpha} = 1 + n \left[\sum_{i=1}^{n} \ln \frac{x_i}{x_{min}} \right]^{-1}. \tag{7}$$

Following the derivation of the MLE PLE in this form, a variant derivation of the same form must be made taking into account the fact that the observations $x_i \geq x_{min}$, representing frequencies in the log-log transformed PSD, are represented in amount equal to the magnitude of the log-log transformed PSD for those frequencies. To represent this, the following relationship is defined:

$$n = \sum_{j=1}^{m} PSD(j) \tag{8}$$

where m is the total number of bins in the PSD and j is the bin index. An important point must be made here: the PSD representation of the spectral activity in the ECoG time series is being interpreted here as a distribution of samples, where the magnitude of the power spectral density at a specific bin represents the total quantity of measured samples of the frequency, x_j, belonging to that PSD bin. Thus, the central term of Equation (7) becomes

$$\sum_{i=1}^{n} \ln \frac{x_i}{x_{min}} = \sum_{j=1}^{m} \mathrm{PSD}(j) \ln \frac{x_j}{x_{min}} \tag{9}$$

Following from Equations (8) and (9),

$$\hat{\alpha} = 1 + \frac{\sum_{j=1}^{m} PSD(j)}{\sum_{j=1}^{m} \mathrm{PSD(j)} \ln \frac{x_j}{x_{min}}} \tag{10}$$

Equation (10) was directly applied to the pre-alpha and post-alpha bands to obtain respective PLE estimates. This derivation is an original contribution and allows for the calculation of a MLE PLE directly from the log-log transformed PSD estimate of the ECoG time series data.

3.4.1.4 Modified Kolmogorov-Smirnov Test for Goodness of Fit

The Kolmogorov-Smirnov (KS) test was used to measure the goodness of fit of a power law, parameterized by the PLE from either the LS or MLE methods, to the PSD data. This test was performed for both methods and for each of the pre-alpha and post-alpha bands. The results of the goodness of fit from this test determines if we can say that the PSD data in each of the bands is sampled from a power law distribution. The results of this test for both methods of PLE estimation were then compared to each other to determine which method provides a better power law fit to the PSD data. The KS test is defined by the following equation (11) below

$$D = \max_{x \geq x_{min}} |S(x) - P(x)| \tag{11}$$

Where $S(x)$ is the cumulative distribution function (CDF) of the data for the observations with value at least x_{min}, and $P(x)$ is the CDF of the power law model that best fits the data in the region $x \geq x_{min}$ [56]. The KS test is known to be more insensitive to differences between CDFs near the limits of 0 and 1. For this reason a modified version of the KS test was used, reweighted to provide uniform sensitivity across the range of the CDF [61]:

$$D^{*} = \max_{x \geq x_{min}} \frac{|S(x) - P(x)|}{\sqrt{P(x)(1 - P(x))}} \tag{12}$$

In literature characterizing ECoG data or EEG data according to power law theory it is uncommon for evidence to be provided supporting the hypothesis that the ECoG spectral structure is distributed according to a power law [56]. In one study in particular, Heathcote et al. demonstrated that averaging caused a bias towards a better fit of a power law to sampled data [62]. Exponential distributions are particularly visually similar to power law distributions on a logarithmic scale. Therefor, for the purpose of demonstrating the differences between the MLE and LS methods of estimating PLE, hypothesis testing was conducted to determine if it was plausible that the PSD data was sampled from a power law distribution. The null hypothesis for each test was that the KS test result for the LS or MLE estimated PLE was larger than a KS test result for a distribution randomly sampled from a power law distribution. A Monte Carlo bootstrapping method was applied to test this hypothesis [63]. For each KS test result (pre-alpha or post-alpha | LS-PLE or MLE-PLE) 2,500 synthetic datasets of power law distributed data were created. These datasets were created by randomly sampling 10,000 points (frequencies) from a power law distribution with a PLE equal to the LS or MLE estimation for the ECoG PSD data. For each of these synthetic datasets, the KS test was performed. Cumulatively, these 2,500 KS test results represent a distribution of likely test results for data that is known to have been sampled from a power law distribution. The number of synthetic datasets and points per dataset were selected to ensure that the p-value was accurate to two decimal digits as in [56]. A KS test result that is significantly larger than the mean of the synthetic KS test result distribution supports the null hypothesis that a power law is not a good fit to the ECoG PSD.

The KS distance was also used as a feature alongside the pre-alpha and post-alpha PLE in the classification of tumorous and healthy tissue using discriminant analysis and support vector machine classifiers. The thought process behind using the KS distance as a feature was that the degree to which the PSD smoothly fits a power law may be different for tumorous and healthy tissue.

3.4.2 Relative Spectral Amplitudes

The amplitudes of specific spectral bands were chosen as features for this work. The bands chosen were the delta band (0-4Hz), alpha band (7-13Hz), beta band (14-30Hz), and gamma band (30Hz+). In this work the gamma band was limited to 30-45Hz. The magnitude of each band in the ECoG PSD was extracted and normalized with respect to the total PSD magnitude in the 0-45Hz range. These magnitude features for each band represent four features used in further classification steps.

3.4.3 Functional Connectivity Features

The PLI and PLV algorithms, along with the linear correlation and magnitude squared coherence (MSC) algorithms, are used in this work to produce features representative of the degree of functional connectivity between electrodes in the ECoG grid. More advanced methods exist to study directed connection between different brain regions or electrode recording sites, for example Granger causality and the Directed Transfer Function [22], but these methods are not studied in this work.

For each of the four functional connectivity features (FCFs) used in this work (PLI, PLV, linear correlation, MSC), two ECoG channels are compared to each other at a time. For the entire grid of at most 32 ECoG electrodes, each electrode is only compared to its immediately adjacent electrodes and a mean result is calculated as the average of the comparisons. A depiction of these comparisons is given below in Figure 5.

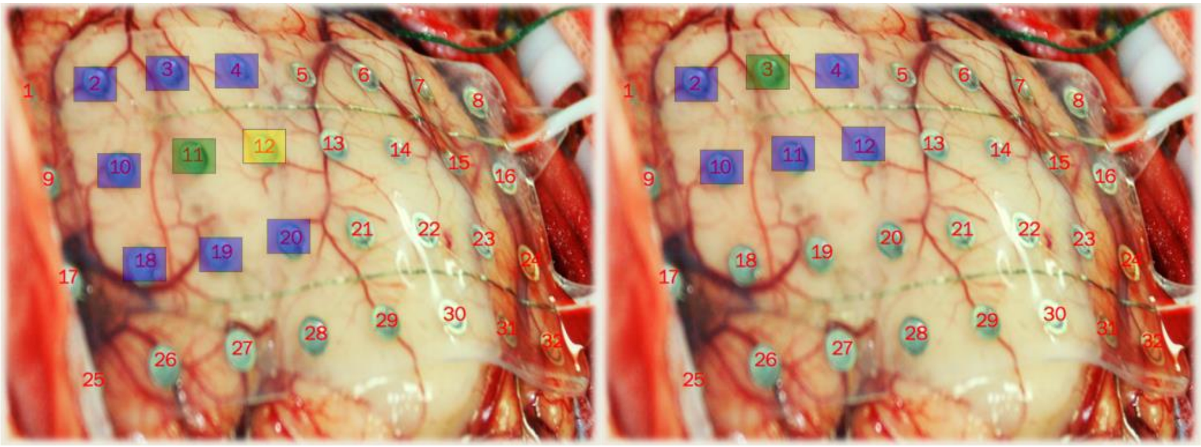

Figure 5: Functional connectivity feature electrode comparisons.
The electrode currently selected for which a functional connectivity feature will be produced is shown in green. Electrodes shown in yellow are poor quality electrodes that have been excluded from the dataset of a subject. Electrodes shown in blue are the higher quality electrodes across which a mean functional connectivity feature is produced. [69]

An important note should be made here: for electrodes bordering the ECoG grid, functional connectivity features were produced for a smaller number of electrodes then would be produced for electrodes in the middle of the ECoG grid. Additionally, poor quality electrodes that were excluded from the datasets in the preprocessing step were not included in the calculation of these FCFs. The effect of this is that FCFs were produced as average representations of different numbers of electrode comparisons.

3.4.3.1 Phase Lag Index

While the linear correlation, MSC, and PLV methods are more prone to bias as a result of volume conduction, the Phase Lag Index (PLI) was designed to avoid this bias [38]. The PLI is the measure of the asymmetry of the of the distribution of the phase differences between two signals.

The ECoG data was separated temporally into four-second epochs following the preprocessing steps explained in section 3.3. Next the Hilbert Transform was applied to each epoch and using the real time series within the epoch and its Hilbert Transform, the analytical signal of the epoch was calculated and the instantaneous phase of that signal produced [21] as given below in equation (13)

$$\varphi(t) = arctan\frac{\tilde{x}(t)}{x(t)}, \tag{13}$$

where $x(t)$ is the real time series from the epoch and $\tilde{x}(t)$ is its Hilbert Transform. For two such phases, θ_1 and θ_2, calculated for different channels but for the same temporal epoch, a phase difference is calculated as in equation (14)

$$\Delta\varphi(t) = \theta_1(t) - \theta_2(t). \tag{14}$$

The PLI is then calculated with this phase difference as [38]

$$PLI = |\langle sign[\Delta\varphi(t)]\rangle| \tag{15}$$

where the $|\quad|$ brackets denote the absolute value, the $\langle\quad\rangle$ brackets denote the mean, and $sign$ denotes the signum function which extracts the sign of its input as either a -1 or a +1. The output of the signum function represents a distribution of binary values either showing a leading or lagging phase comparison for each temporal sample of the phase difference. Averaging this distribution produces a mean value representing the magnitude and direction of phase lag between the two signals of comparison, and then the absolute value of this represents only the magnitude information related to the phase lag. A PLI of 1 indicates perfect phase locking while a PLI of 0 indicates no phase locking. With a PLI calculated for each epoch within each ECoG data channel, an average PLI was calculated for each channel by averaging across all PLI calculations within a channel.

3.4.3.2 Phase Locking Value

The Phase Locking Value was created as a means to measure coordinated activation over different brain regions [25]. This algorithm separates the phase of the signal from its magnitude and was originally proposed as a connectivity measure by Lachaux et al. [39].

Following the preprocessing in section 3.3, a 4th order Butterworth bandpass filter with a passband 30-40Hz was applied to the ECoG dataset to investigate gamma-related phase locking activity. The entire temporal length of the dataset was split into four-second epochs as it was for the PLI calculation above in section 3.4.3.1. The Hilbert Transform was applied to each epoch and using the real time series within the epoch and its Hilbert Transform, the analytical signal of the epoch was calculated and the instantaneous phase of that signal produced [21] as given in equation (13). For two such phases, θ_1 and θ_2, calculated for different channels but for the same temporal epoch, a phase difference is calculated as in equation (14).

The PLV is then calculated as

$$PLV_n = \frac{1}{T}\left|\sum_{t=1}^{T} \exp\left(j\Delta\varphi(t,n)\right)\right| \tag{16}$$

where $n[1,\dots,N]$ is the epoch number and $t[1,\dots,T]$ is the sample index within each epoch. The PLV for each channel was produced by averaging the PLV value across all epochs.

3.4.3.3 Magnitude Squared Coherence

The magnitude squared coherence is defined as

$$C_{xy}(f) = \frac{\left|P_{xy}(f)\right|^2}{P_{xx}(f)P_{yy}(f)} \tag{17}$$

where $P_{xx}(f)$ and $P_{yy}(f)$ are the PSDs of each of the two signals being compared and $P_{xy}(f)$ is the cross power spectral density. A value of 0 corresponds to total asynchrony and a value of 1 corresponds to perfect synchrony. Specific frequency bands need to be selected for the calculation of this FCF. For this work, and for the purpose of comparing results to the work of Boussen et al, two different frequency bands were selected: 0-4 Hz (low band) and 4-40 Hz (high band). Following the preprocessing in section 3.3, a 2nd order Butterworth bandpass filter was applied to the ECoG dataset to isolate either the low or high band from the spectral content. The ECoG data was then split into 20-second epochs and the MSC for each epoch calculated as a mean MSC across all frequencies within either the low or high band, and the MSC for each channel calculated as the mean MSC across all MSC results for each electrode pair comparison as illustrated in **Figure 5**. The MATLAB function ‘mscohere’ was used to calculate all MSC values.

3.4.3.4 Linear Amplitude Correlation

The Linear Amplitude Correlation (LAC) FCF is defined as the Pearson Correlation Coefficient [64]

$$\rho(A,B) = \frac{1}{N-1}\sum_{i=1}^{N}\left(\frac{A_\imath - \mu_A}{\sigma_A}\right)\left(\frac{B_i - \mu_B}{\sigma_B}\right) \tag{18}$$

where μ_A and σ_A are the mean and standard deviation, respectively, of time series A and μ_A and σ_A are the mean and standard deviation, respectively, of time series B. For the work presented in this thesis, the LAC was calculated according to the above Equation (18). It should be noted here that electrocorticographic data presents with nonstationary dynamics and thus is not accurately represented by a mean value or standard deviation within a specific, fixed time window [65]. Nonetheless, the LAC has been widely applied in literature to ECoG and EEG data.

3.5 Tissue Classification

Multiple classification methods were employed independently to evaluate the utility of multiple features in the identification of ECoG electrode data as tumorous data or healthy data. Linear discriminant analysis (LDA), quadratic discriminant analysis (QDA), and support vector machines (SVM) were used to classify electrode channels as tumorous or healthy using only PLE and KS test features. K-fold cross validation was used to measure the performance of these classifiers. An artificial neural network (ANN) was also designed for classification using the features demonstrating maximal separability between tumorous and healthy classes. The primary feature of interest for this work is the PLE. As such, for the purpose of evaluating its potential utility in classification algorithms, out of the three classes of tissue contained in the ECoG dataset (healthy, peritumoral, and tumorous) only healthy and tumorous tissue classes were studied for classification performance. The classification methods used in this work represent a basic set of supervised classifiers that are very commonly used and discussed in literature.

3.5.1 Discriminant Analysis and Support Vector Machines

The two discriminant analysis methods employed in this work for classification of tumorous and healthy tissue classes are the LDA and the QDA. The assumptions that are made in the application of discriminant analysis are that the class conditional densities are approximately normal and that the sampled features are good estimates of the population features [44]. The probability density used in this assumption is given as

$$f_k(\boldsymbol{X}) = (2\pi)^{-p/2}|\Sigma_k|^{-1/2} exp\left[-1/2(\boldsymbol{X}-\boldsymbol{\mu_k})^T {\Sigma_k}^{-1}(\boldsymbol{X}-\boldsymbol{\mu_k})\right] \tag{19}$$

[44] where k is the class, $\boldsymbol{X}$ is the set of measurements, and Σ_k and $\boldsymbol{\mu_k}$ are its covariance matrix and mean, respectively. The loss function for discriminant analysis is specified as

$$L(k,\hat{k}) = 1 - \delta(k,\hat{k}) \tag{20}$$

with the loss associated with an incorrect class assignment given as

$$R(\hat{k} \mid \boldsymbol{X}) = \frac{\sum_{k=1}^{K} L(k,\hat{k}) f_k(\boldsymbol{X})\pi_k}{\sum_{k=1}^{K} f_k(\boldsymbol{X})\pi_k} \tag{21}$$

where π_k is the unconditional prior probability of observing the class k. This equation then reduces to

$$f_{\hat{k}}(\boldsymbol{X})\pi_{\hat{k}} = \max_{1\le k\le K} f_k(\boldsymbol{X})\pi_k \tag{22}$$

which leads to the classification rule

$$d_{\hat{k}}(\boldsymbol{X})\pi_{\hat{k}} = \min_{1\le k\le K} d_k(\boldsymbol{X}) \tag{23}$$

with

$$d_k(\boldsymbol{X}) = (\boldsymbol{X}-\boldsymbol{\mu_k})^T {\Sigma_k}^{-1}(\boldsymbol{X}-\boldsymbol{\mu_k}) + \ln|\Sigma_k| - \mathbf{2}\ln\pi_k \tag{24}$$

which is called the discriminant score for the k^{th}class. Using the above two equations is called quadratic discriminant analysis and when the class covariance matrices are presumed to be identical the equations instead define linear discriminant analysis [44]. The MATLAB *fitcdiscr* function was used to train linear discriminant models using the PLE and KS distance as features. The LDA method produces a model that separates classes with a linear function, whereas the QDA produces a model that separates classes using a quadratic model.

Support Vector Machines (SVMs) were used classify tumorous and healthy tissue in addition to the discriminant methods. While the mathematical equations underlying the SVM theory will not be discussed here, some of the basic SVM concepts will be presented in **Figure 6** below.

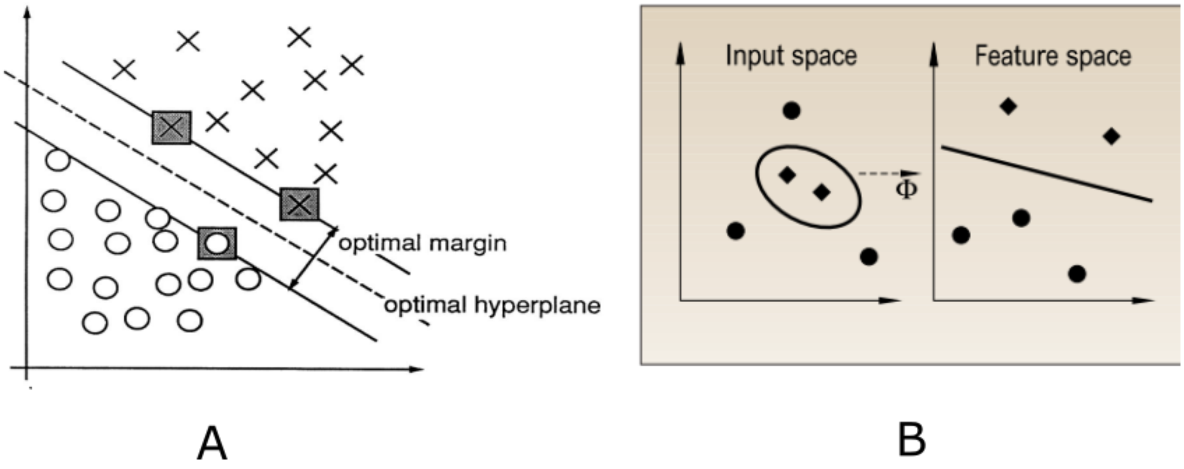

Figure 6: Support Vector Machine Basic Concepts.
(A) presents the concept of margin between a hyperplane and the data points lying on the edge of the margin, called the support vectors. The optimal hyperplane is achieved by maximizing the margin. (B) Illustrates the utility of a kernel. The SVM kernel is used to transform an input feature into a higher order feature space with optimal separability between classes. [46] [47]

The SVM method finds a hyperplane lying between two classes. The optimal hyperplane lies orthogonal to the optimal margin between classes. Data points lying directly on the margin edge are called the support vectors [46]. Different kernel functions are used to map an input feature space nonlinearly into a higher dimensional feature space where a hyperplane can be created between two classes with maximum margin [47]. The MATLAB function *fitcsvm* was used to train a SVM model on the tumorous/healthy class data. Radial Basis Functions (RBFs) were chosen for the kernel functions.

3.5.1.1 Cross Validation

Following the training of discriminant models and SVM models, 10-fold cross validation was used to measure the performance of the models in the classification of the healthy/tumorous data. This method splits the data observations into 10 different groups, training a model using nine 9/10 groups while using the other 1/10 groups to test the classification of the model. The MATLAB function *crossval* was used to cross-validate the models while *kfoldLoss* was subsequently used to return the fraction of misclassified data.

3.5.2 Artificial Neural Network

An artificial neural network (ANN) was designed and used to classify tumorous and healthy data in addition to the discriminant and SVM methods. The mathematical basis of ANNs will not be discussed here in detail; the reader will find these details in [66]. The architecture of the ANN is depicted below in **Figure 7**.

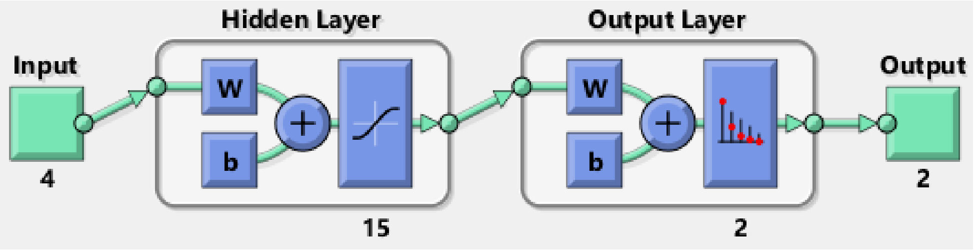

Figure 7: ANN Architecture.
Four total features were used as inputs: pre-alpha PLE, post-alpha PLE, PLI, and MSC-High. The number of hidden neurons were set to 15 and the number of output neurons is set to 2.

A two-layer feed forward network was designed using the Neural Network Pattern Recognition app from the MATLAB Deep Learning Toolbox. Four features were chosen as input: pre-alpha PLE, post-alpha PLE, PLI, and MSC-High. The number of neurons in the hidden layer was set to 15. The number of outputs was set to 2 for healthy/tumorous tissue classification. A sigmoid transfer function was used in the hidden layer and a softmax transfer function was used in the output layer. Scaled conjugate backpropagation was used as the training algorithm. 70% of the input samples were used for training, 15% for validation, and 15% for testing. The design chosen for this ANN was meant to compare directly to the design of the ANN used by Boussen et al. 2016 [25], for which some of the same features were used to achieve decent classification performance in the identification of tumorous neural tissue.

4. Results

4.1 Labelled Subject Data

Following the data preprocessing step and subsequent removal of ECoG electrode channels identified to be poor quality, 447 channels were retained across all 17 subjects. Of these channels, 144 were healthy, 128 were peritumoral, and 175 were tumorous. The labelled electrode maps for all subjects are shown below in **Figure 8**.

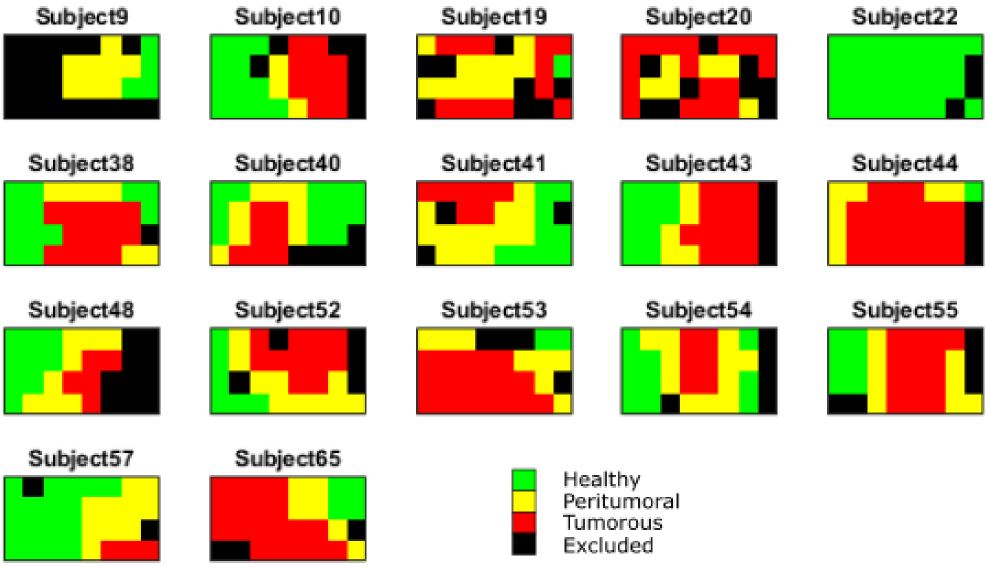

Figure 8: Electrode Labelling.
All labelled electrodes are depicted here, colored according to the label each electrode was given: Healthy, Peritumoral, Tumorous, and Excluded. Each electrode is represented by one tile in the colormap for each subject.

4.2 PLE: The Effect of CGSA

The effect the CGSA had on the spectral structure of the PSD is shown below in **Figure 9**. The CGSA-processed PSD is shown in this figure as well, along with both LS and MLE power law distributions for both pre-alpha and post-alpha bandwidths.

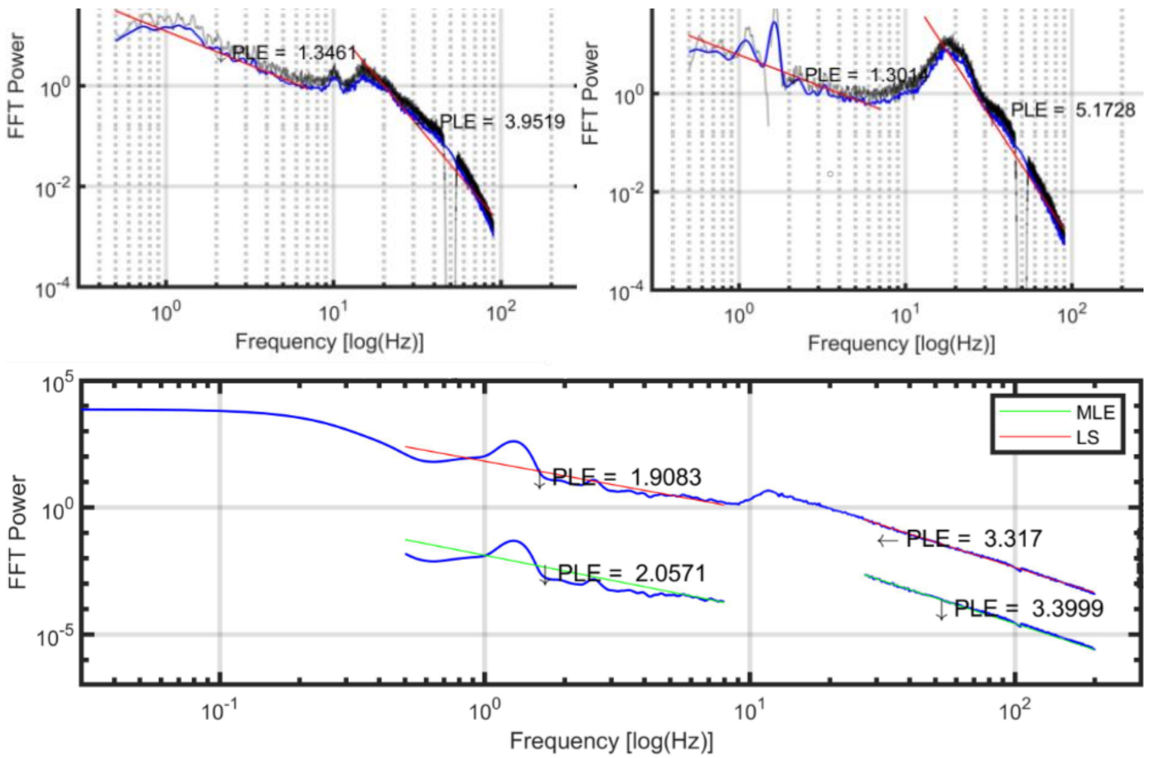

Figure 9: The Effect of CGSA on Spectral Structure.
Two example representative PSD comparisons are shown. The PSD is shown here in black with the CGSA-PSD shown here in blue.

CGSA appeared to slightly reduce the amplitudes of harmonic peaks within the PSD. The overall appearance of the effect of CGSA is that of a smoothing filter. The CGSA-PSD structures still have large harmonic peaks and it was not expected that the PSD and CGSA-PSD would be as structurally similar as they are. The same observation, pertaining to the absence of a large harmonic-reduction effect of CGSA, was noted by He et al. in their work [26]. The remaining harmonic peaks within the pre-alpha band appear to be large enough that they are expected to have a large influence on PLE estimates.

4.3 PLE: Goodness of Fit

The goodness of fit tests, measured using the KS distance and averaged over all channels, are shown below in Figure **10**.

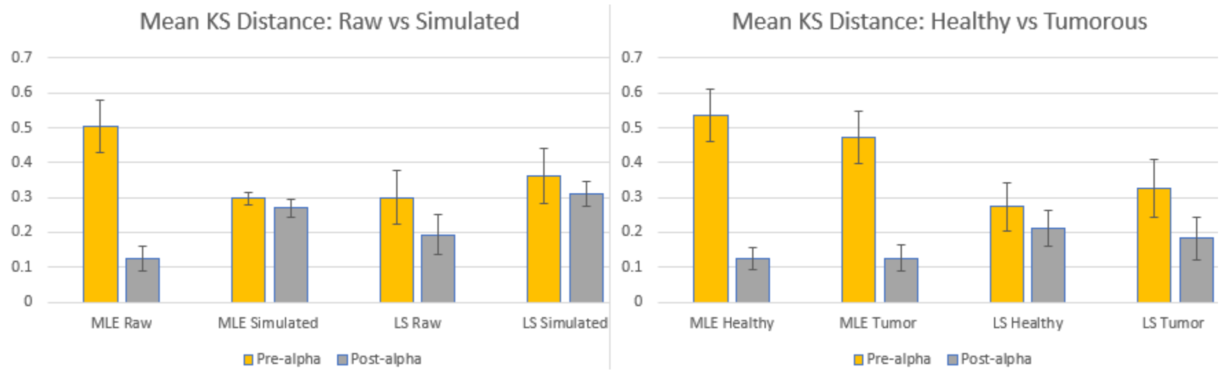

Figure 10: Mean KS Distances.
Pre-alpha KS distances are shown in yellow and post-alpha KS distances shown in grey. The bar chart on the left side depicts the comparison between KS distances from measured PSD data and KS distances from simulated PSD data. The bar chart on the right depicts the KS distance comparison between healthy tissue and tumorous tissue for both LS and MLE methods.

The pre-alpha KS distances were all larger than the post-alpha KS distances. For the MLE method the pre-alpha healthy tissue KS distances were much larger than the post-alpha healthy tissue distances. Observation of the PSD examples in **Figure 9** present the visual distinction between pre-alpha and post-alpha bandwidths. As the pre-alpha bandwidths tend to have larger and wider harmonic peaks, it is expected that the goodness of fit of a power law to this bandwidth will be less than that of the post-alpha PLE. For the better-fit post-alpha band, both MLE Raw and LS Raw KS distances are smaller than their ‘Simulated’ counterparts, MLE Simulated and LS Simulated, respectively. This suggests that the power law was a better fit to the raw data in the post-alpha band than it was to data that was randomly sampled from a power-law distribution. This in turn suggests that the post-alpha band data is structured according to a power law. Additionally, for the post-alpha band, the MLE Raw KS distance is nearly half as small as the LS Raw KS distance. The MLE simulated data also had a smaller KS distance than the LS simulated data. These facts suggest that The MLE method of fitting a power law produces a better fit, and therefor better estimate of the PLE, than the LS method does. For the pre-alpha band the MLE Raw KS distance was larger than the simulated and outside the range of its one standard deviation, suggesting that random sampling from a power law distribution would not produce data as poorly fit as it is. The LS method did not produce a KS distance for the raw data larger than for the simulated data. This suggests that the LS method is less sensitive to harmonic peaks through the band which a power law is being to.

The KS distances for healthy and tumorous tissue appear to be relatively similar for both LS and MLE methods. This suggest that as a feature, the KS distance does not offer information that would contribute to better classification of tumorous tissue.

4.4 PLE: Tissue Distributions and Statistical Testing

The distributions of PLE for both LS and MLE estimation methods and for both the pre-alpha and post-alpha spectral bandwidths, are shown below in **Figure 11**.

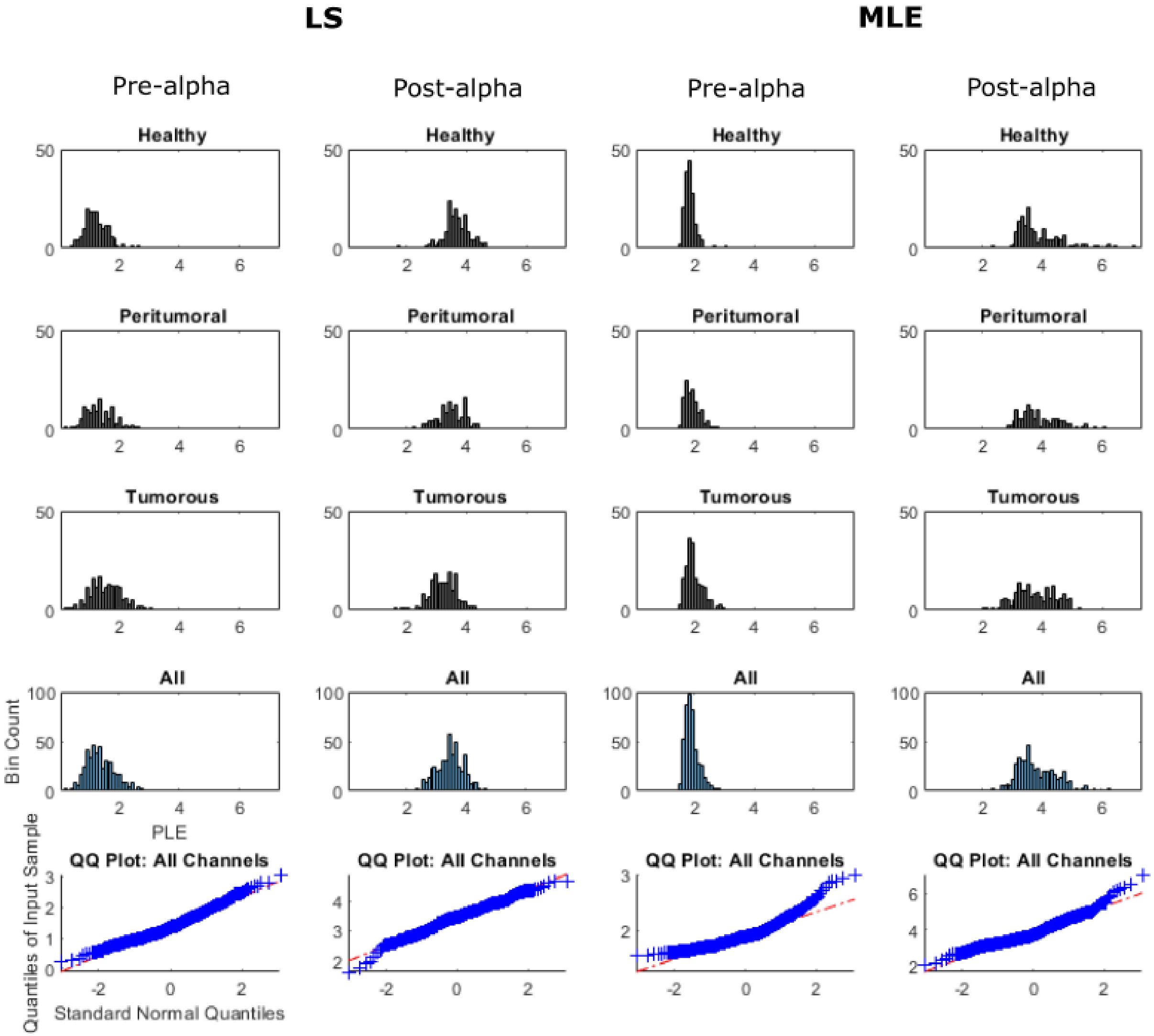

Figure 11: PLE Distributions.
Shown here are the PLE distributions for all channels included in the dataset (159 Healthy, 123 Peritumoral, 179 Tumorous). Distributions are shown for both LS and MLE methods, and for each method the pre-alpha and post-alpha distributions are given.

For LS-pre-alpha, LS-post-alpha, and MLE-post-alpha distributions, the sample quantile versus standard normal quantile ‘QQ’ plots all show a close fit between the sample and standard normal distributions while for the MLE-pre-alpha distributions, there is a clear variance of the sample quantiles away from the standard normal quantiles. The MLE pre-alpha distributions do not appear normal and are visually distinct from the other distributions. The MLE post-alpha distributions appear to have larger variances than the LS distributions. Looking at the distributions for all tissue types, it appears that the LS distributions are more normal than the MLE distributions. All tissue type distributions under the MLE pre-alpha and MLE post-alpha categories appear to have the same mean value and similar variances. On the other hand, for the LS pre-alpha case, the tumorous tissue PLE appears to have a slightly larger mean and variance. For the LS post-alpha case the tumorous tissue PLE appears to have a slightly smaller mean PLE and similar variance to the healthy tissue. Peritumoral tissue PLE appears to be represented somewhere between the healthy and tumorous distributions for both the pre-alpha and post-alpha bandwidths. The MLE and LS post-alpha distributions appear to have similar mean PLE values however their variances are visibly different, with the LS variance skewing to the lower side and the MLE variance skewing more to the higher side. For both MLE and LS methods, pre-alpha PLE is distributed around a lower mean value than the post-alpha distributions are. This is an expected outcome following from the observation of **Figure 9**, where one can clearly identify a slope change in the PSD structure between the pre-alpha and post-alpha distributions.

The box plot representations of the distributions shown in **Figure 11** are shown in **Figure 12**.

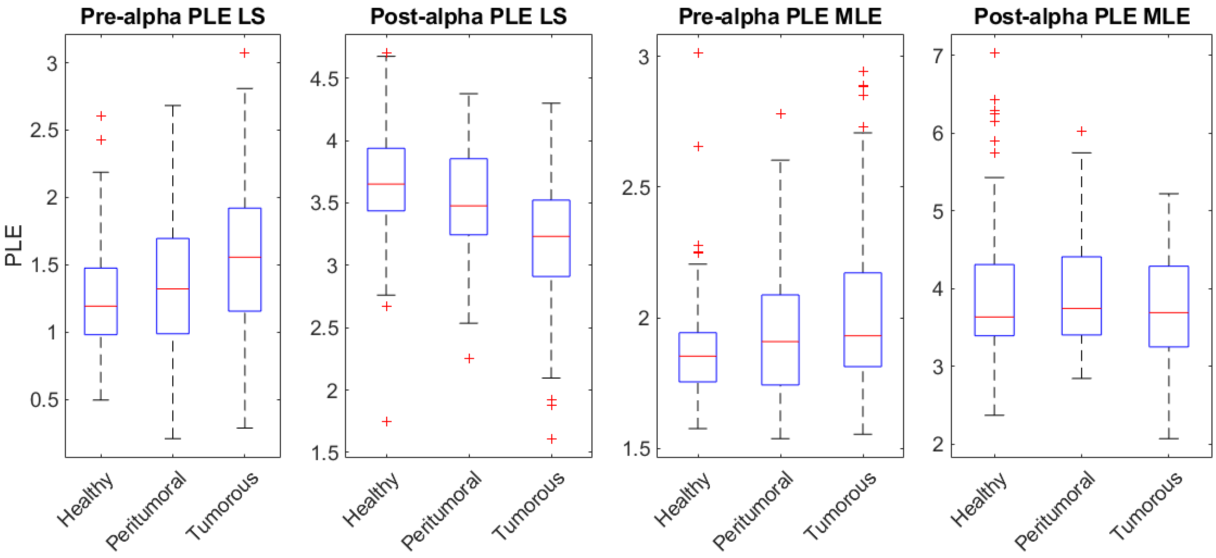

Figure 12: PLE Box Plots.
Healthy, Peritumoral, and Tumorous box plots are shown for comparison of the PLE of all tissue types within each independent PLE set. Outlier data points are shown with red '+' signs.

The box plot representations of the LS method PLE distributions illustrate more clearly the differences between the tissue type PLEs. For the LS pre-alpha case, healthy PLE was the lowest, with the smallest variance. The tumorous PLE was the highest and had a larger variance. For the LS post-alpha case, healthy tissue had the largest PLE and smallest variance while tumorous tissue had the smallest PLE and a larger variance. For both LS pre-alpha and post-alpha cases, the peritumoral PLE lies between the healthy and tumorous PLEs. In the case of the MLE method of estimating PLE, all post-alpha tissue PLEs appear to be very similar, however there are a large number of outliers in the healthy PLE distribution. For MLE pre-alpha, healthy tissue appeared to have the smallest PLE and tumorous tissue the largest.

Student's t-test was applied to compare the healthy and tumorous tissue distributions with the null hypothesis that both distributions have the same mean PLE. The t-test was applied using MATLAB's '*ttest2*' function with the assumption that the distributions have unequal variances. Comparisons involving the peritumoral tissue PLE were not made because healthy and tumorous tissue were the only two tissue types of interest for classification within this work. The results of these statistical tests are shown below in **Table 3**.

Table 3: PLE Distribution Parameters and Statistical Test Results.
Healthy and tumorous tissue types are compared in the table below using Student's t-test with the assumption of unequal variances.

	Mean PLE	PLE variance	p-value
LS prealpha healthy	1.235	0.136	**** $1.302\text{x}10^{-10}$
LS prealpha tumorous	1.558	0.270	
LS postalpha healthy	3.676	0.178	**** $6.224\text{x}10^{-20}$
LS postalpha tumorous	3.214	0.203	
MLE prealpha healthy	1.865	0.035	**** $1.291\text{x}10^{-07}$
MLE prealpha tumorous	2.003	0.078	
MLE postalpha healthy	3.925	0.586	* 0.0276
MLE postalpha tumorous	3.750	0.446	

The acceptable probability of Type-I error in the above statistical tests was chosen to be $\alpha = 0.05$. Bonferroni corrections were not applied due to single comparisons being applied to independent sampled data.

The LS pre-alpha PLE of tumorous tissue is significantly larger than that of healthy tissue. The LS post-alpha PLE of tumorous tissue is significantly smaller than that of healthy tissue. For the MLE method, pre-alpha tumorous PLE was significantly larger than that of healthy tissue and the post-alpha tumorous PLE was barely significantly smaller than that of healthy PLE. Both methods of PLE estimation show that healthy PLE is significantly different from tumorous PLE, although the LS method more clearly demonstrates this difference. While healthy tissue PLE distributions for pre-alpha and post-alpha bands are more distant from each other, tumorous tissue PLE distributions are less distant from each other. The closer proximity of the tumorous distributions to each other can be seen below in **Figure 13**.

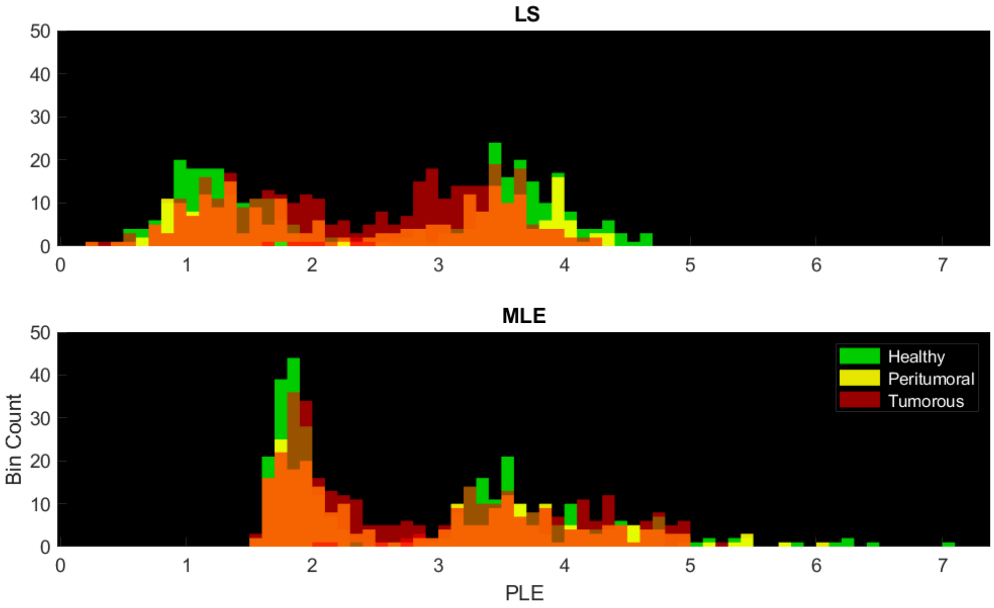

__Figure 13: Combined Pre-alpha and Post-alpha PLE Distributions.__
Pre-alpha and post-alpha PLE are both shown as a single distribution for each of the LS (top) and MLE (bottom) methods.

Using the LS method of estimating PLE, healthy tissue appears to be more visually distinct from tumorous tissue. For all three tissue types, the PLE distributions of the MLE estimator appear to be very similar whereas they do not appear to be as similar for the LS estimator. Of a particularly important note, the tumorous tissue distributions of LS pre-alpha and LS post-alpha PLE appear to be conjoining, and some of the samples of each distribution could be contained by the other one. This raises the question of if tumorous tissue PSD structures can be characterized by a singular PLE instead of the two PLEs that are necessary for characterizing healthy tissue PSDs.

A representative view of the finding that LS post-alpha healthy tissue has a larger PLE than LS post-alpha tumorous tissue, is shown below in **Figure 14**.

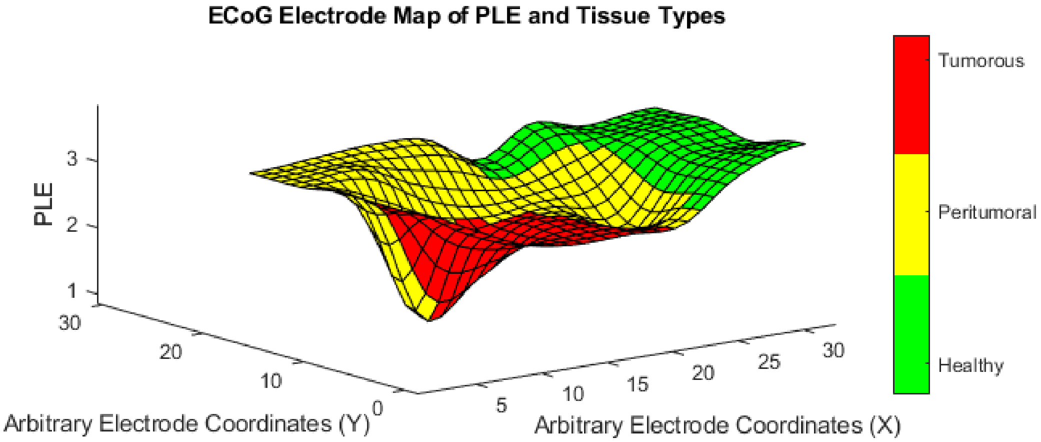

Figure 14: Topographical Map of ECoG grid PLE.
PLE values are shown here for the electrode grid of one example subject, subject 41. The ECoG grid is represented with an increased, interpolated resolution to smooth the actual ECoG electrode PLE values such that visual interpretation is easier. The scale in this figure is representative of the 4x8 ECoG array used for measurement.

This example subject, subject 41, clearly visualizes the relationship between PLE and tissue type. The peritumoral tissue clearly bears similarity to healthy and tumorous tissue with respect to PLE magnitude. This example subject's PLE topography can be compared directly to its electrode labelling map shown in **Figure 8**.

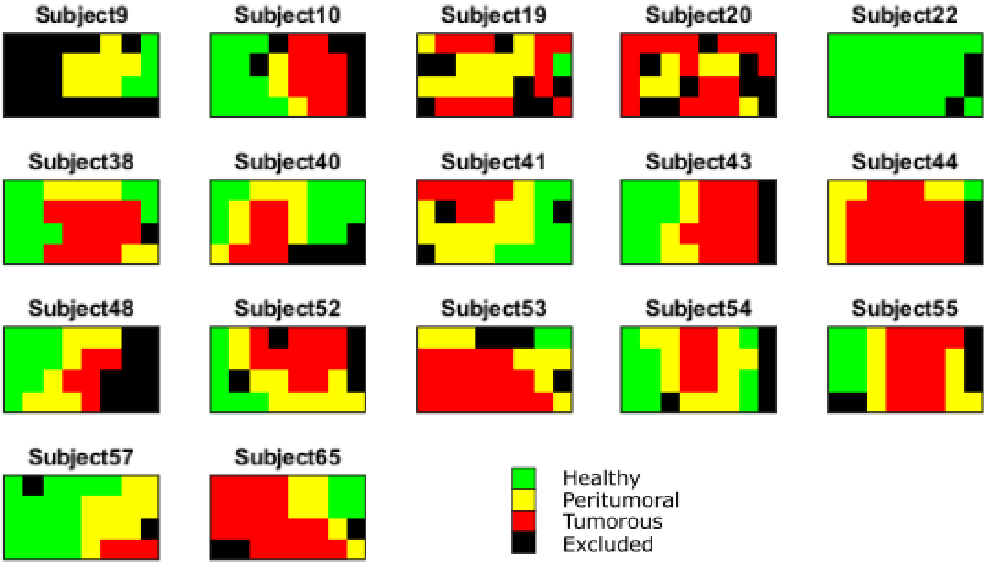

Figure 15: Electrode Labelling.
All labelled electrodes are depicted here, colored according to the label each electrode was given: Healthy, Peritumoral, Tumorous, and Excluded. Each electrode is represented by one tile in the colormap for each subject.

The LS PLE data for all subjects, colored for tissue type, is shown below in **Figure 16**.

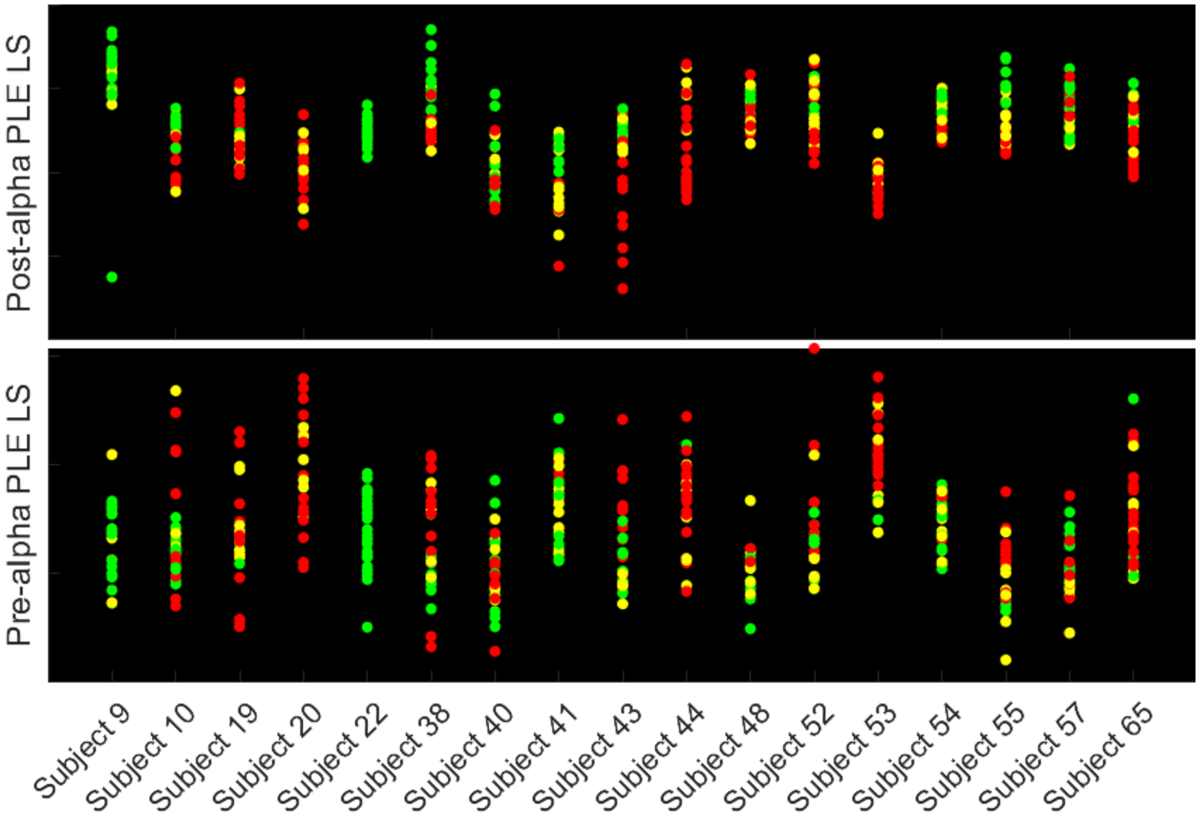

Figure 16: Subject-wise PLE LS Distributions.
All Channel PLE estimates are given in this figure for each subject, color coded for tissue type. Healthy tissue is shown in green, peritumoral in yellow, and tumorous in red. Post-alpha PLE LS estimates are shown on top and pre-alpha PLE LS estimates are shown on bottom.

It is observed in **Figure 16** that for the post-alpha PLE case, for most subjects with both healthy and tumorous channels, most healthy tissue PLE estimates are higher than tumorous tissue PLE estimates. Furthermore, for the pre-alpha PLE case, for most subjects with both healthy and tumorous channels, most healthy tissue PLE estimates are lower than tumorous tissue PLE estimates.

4.5 Spectral Amplitudes

The distributions of the spectral amplitudes, for all four bandwidths (delta, alpha, beta, and gamma), are shown below in **Figure 17**.

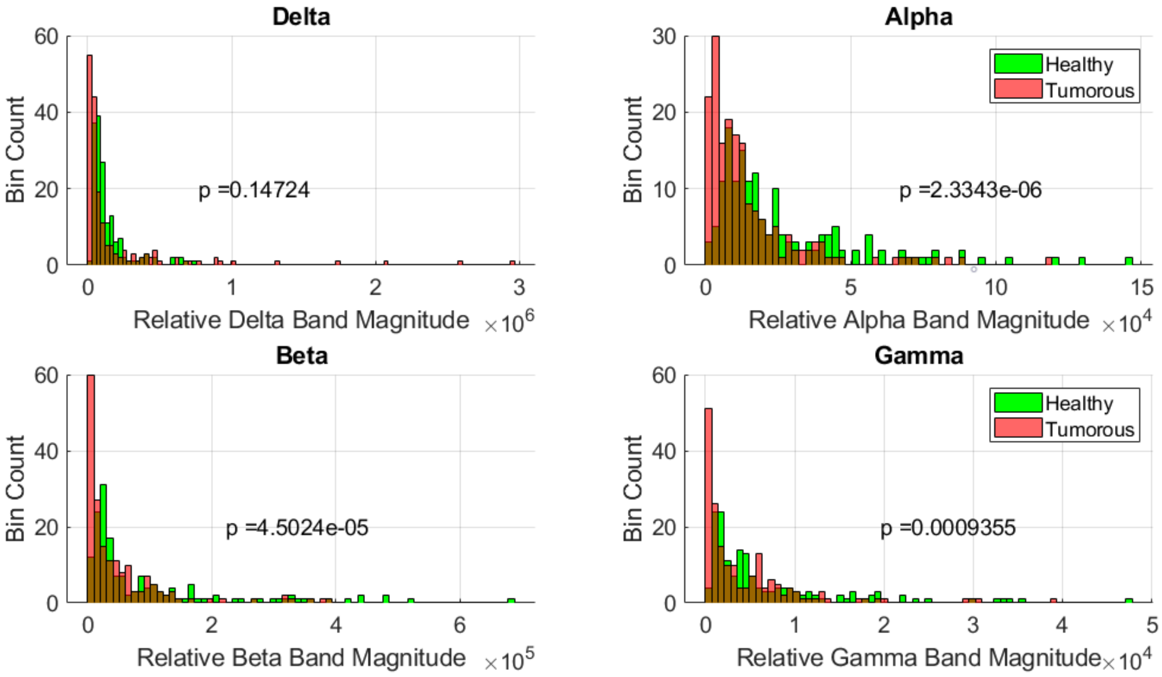

Figure 17: Spectral Amplitude Distribution.
Healthy tissue normalized spectral amplitude bins are shown in blue and tumorous tissue spectral amplitude bins are shown in orange. All four spectral bands (delta, alpha, beta, and gamma) used in this work are shown here.

While all tumorous tissue band power distributions appear to resemble exponential distributions, all healthy tissue band power distributions more closely resemble log-normal distributions. The clearest visual differences between healthy and tumorous tissue are apparent for alpha and beta distributions. These bandwidths (alpha 7-13Hz, beta 14-30Hz) are particularly interesting because the PLE estimations were made outside of these bandwidths. Any information in the alpha and beta bandwidths that lead to discrimination between tissue types, is very likely independent from the information contained in the PLE estimates. The Student's t-test, assuming unequal variance, was used to measure differences between healthy and tumorous band powers and significant differences were found in the alpha ($p = 2.334x10^{-6}$), beta ($p = 4.502x10^{-5}$), and gamma ($p = 2.334x10^{-6}$) bands but not the delta band. The number of samples (159 healthy, 179 tumorous) compared for the t-tests was large; although the distributions were clearly not normal, it was deemed acceptable to use the t-test for testing if the distributions were likely from the same population distribution. The alpha, beta, and gamma bands were deemed valuable for further classification due to the significant differences between their tissue type distributions.

4.6 Phase Lag Index

The Phase Lag Index (PLI) distributions for healthy and tumorous tissue are shown below in **Figure 18**.

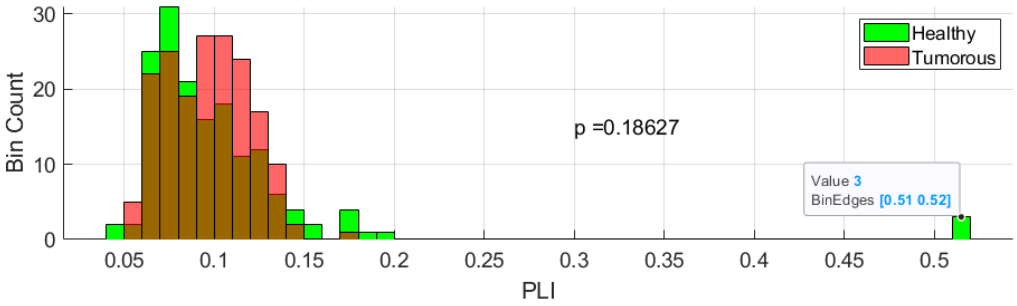

Figure 18: Phase Lag Index Tissue Distribution.
The PLI distributions for healthy and tumorous tissue are presented in the bottom row in blue and orange, respectively. Tumorous tissue was found to have a significantly larger PLI than healthy tissue.

Healthy and tumorous tissues appear to have relatively normal distributions. The distributions of both tissue types are in the low range of the PLI (< 0.2), suggesting that there is a low amount of phase locking activity across electrode channel data. Healthy PLI appears to be distinctly smaller than tumorous PLI. A Student's t-test, assuming unequal variance, was applied to the healthy and tumorous distributions. It was found that there were no significant differences between the two tissue type distributions. This can most likely be attributed to the similarity in their variances, as the means of the two distribution appear to be slightly different. Due to not finding significant differences between the distributions of the two tissue types, the PLI was not used in further classification.

4.7 Phase Locking Value

The phase locking value (PLV) distributions for healthy and tumorous tissue are shown below in **Figure 19**.

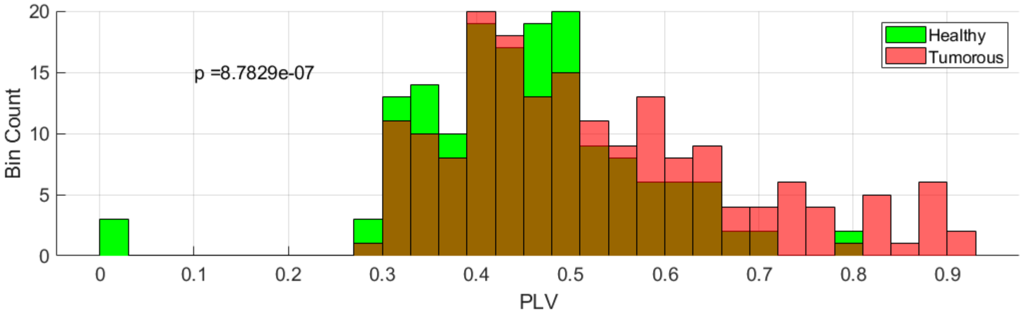

Figure 19: Phase Locking Value Distributions for Healthy and Tumorous Tissue.
In the range of 0.3-0.7 PLV appears to be similarly distributed between the two tissue types. A significant difference was found between healthy and tumorous tissue types; tumorous tissue had a higher PLV than healthy tissue. This is likely attributed to the tumorous PLV samples skewed towards the high PLV range.

While the healthy PLV distribution appears to be relatively close to being normal, whereas the tumorous PLV distribution is less so. The tumorous PLV distribution has a larger number of samples that are skewed towards higher PLV that healthy PLV, indicating that there is more phase locking occurring in tumorous tissue than there is in healthy tissue. The student's t-test was used to investigate the differences between healthy and tumorous PLV. The mean tumorous PLV is significantly ($p = 8.783x10^{-7}$) larger than the mean healthy PLV. For this reason, the PLV is a feature that can be considered valuable in the classification of tumorous tissue. Of particularly important note here is that the phase locking measured is for the 30-40Hz band only, between adjacent channels.

4.8 Magnitude Squared Coherence

The low (0-4Hz) Magnitude Squared Coherence (MSC) distributions for healthy and tumorous tissue are shown below in **Figure 20**.

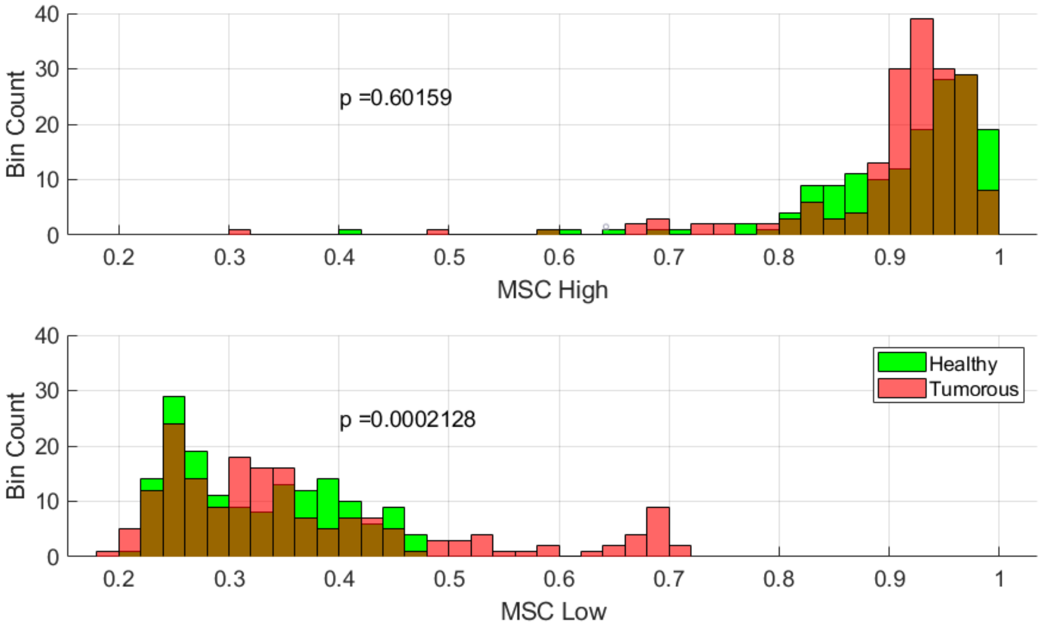

Figure 20: Magnitude Squared Coherence (Low) Tissue Distributions.
The magnitude squared coherence in the 0-4Hz "Low" band is shown here in the bottom row. The magnitude squared coherence in the 4-40Hz "High" band is shown here in the top row. Significance of the differences between the distributions is given in the respective plots.

The distributions of MSC-Low and MSC-High appear non-normal. The MSC-High is distributed through the top of the MSC range while the MSC-Low is more evenly distributed through the bottom half of the MSC range. This suggests that while higher bandwidth activity is very coherent between adjacent electrodes, lower bandwidth activity is not. For MSC-High, the mean values of the tumorous and healthy distributions appear to be slightly different, however their variances do not appear very different. For MSC-Low, the healthy distribution clearly has a smaller variance than the tumorous distribution which has many samples spread through the 0.5-0.7 range where healthy tissue does not. Student's t-test was applied to both MSC-High and MSC-Low with the null hypothesis that both tissue type distributions have the same mean value. It was found that there are significant differences between healthy and tumorous tissue for the MSC-low case ($p = 0.0002$) but not for the MSC-High case ($p = 0.602$). For this reason, MSC-Low was deemed to be a valuable feature for use in classification in this work.

4.9 Linear Amplitude Correlation

The distributions of Linear Amplitude Correlation (LAC) for healthy and tumorous tissue are shown below in **Figure 21**.

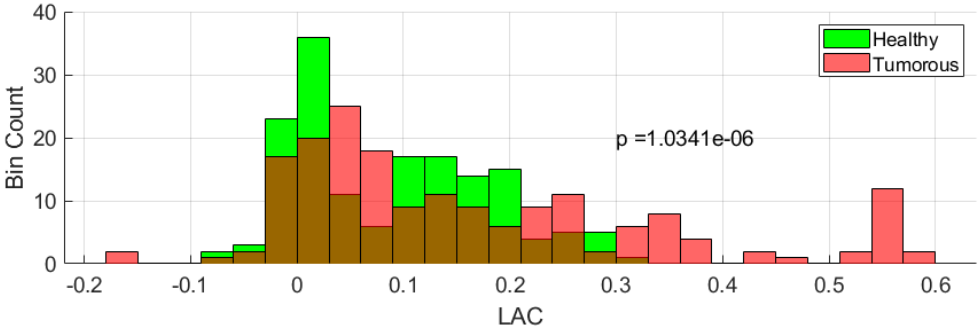

Figure 21: Linear Amplitude Correlation Distributions for Healthy and Tumorous Tissue.
Healthy tissue is shown in green and tumorous tissue is shown in red. A significant difference was found between healthy tissue LAC and tumorous tissue LAC ($p = 1.034x10^{-06}$)

The healthy and tumorous tissue LAC distributions are spread across the positive lower half of the range of possible LAC values. This suggests that neither tissue type has highly correlated activity between adjacent neighbours. Healthy tissue LAC has a smaller variance than tumorous tissue LAC, tumorous tissue appearing to be more flattened out across a wide range of values and with more samples showing more highly correlated activity than for the healthy tissue. The student's t-test was used to study the differences between tissue type LAC. It was found that the mean tumorous tissue LAC is significantly larger than the mean healthy tissue LAC. This suggests that the two tissue types do not come from the same population distribution and that there is useful information within the LAC for classifying tumorous tissue. For this reason, LAC was used in the classification methods studied in this work.

4.10 Classification Performance

The discriminant classifiers were trained and tested using only the post-alpha and pre-alpha features. The performance of these classifiers, as well as their decision boundaries, is given below in **Figure 22**.

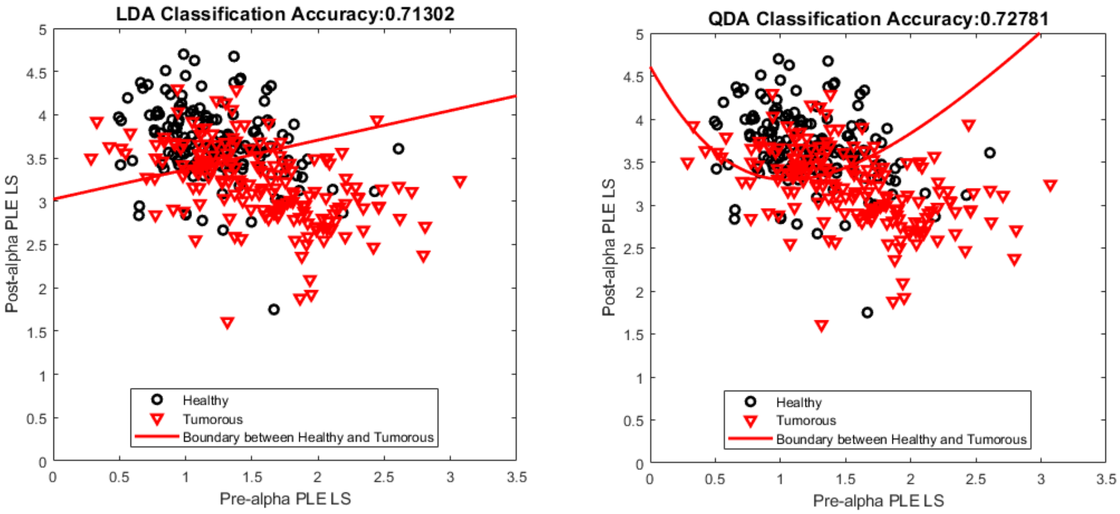

Figure 22: Discriminant Analysis Classification Results.
Healthy and Tumorous tissue post-alpha PLE and KS were used as two features for input to an LDA and a QDA classifier. Classification performance was very similar, nominally 70% for both methods. The PLE-KS feature space with the LDA discriminant plotted suggest that KS distance is not a useful feature in the classification of tumorous tissue.

The performance of the LDA and QDA classifiers, using only the pre-alpha and post-alpha PLE, were very similar, nominally 71% for the LDA and 73% for the QDA. While the distribution of the healthy tissue feature space appears highly normal, the feature space of the tumorous tissue does not. Healthy and tumorous tissue are partially co-located within this feature space and this is likely the cause of the classification performance not being higher.

A SVM was trained on the pre-alpha PLE and post-alpha PLE. The classification accuracy of this SVM was 73.0%. The SVM was retrained with the pre-alpha PLE, post-alpha PLE, LAC, MSC-Low, PLV, Alpha, Beta, and Gamma feature set, and the classification accuracy was also 73.0%. A third SVM was trained using the LAC, MSC-Low, PLV, Alpha, Beta, and Gamma feature set. This third SVM classification accuracy was 71%. All three SVM models perform very similarly and features beyond pre-alpha and post-alpha PLE appear to not add a large amount of useful information for the classification of tumorous tissue.

An ANN was trained on the pre-alpha PLE, post-alpha PLE, LAC, MSC-Low, PLV, Alpha, Beta, and Gamma feature set. The performance of this ANN model is shown with the confusion matrix below in **Figure 23**.

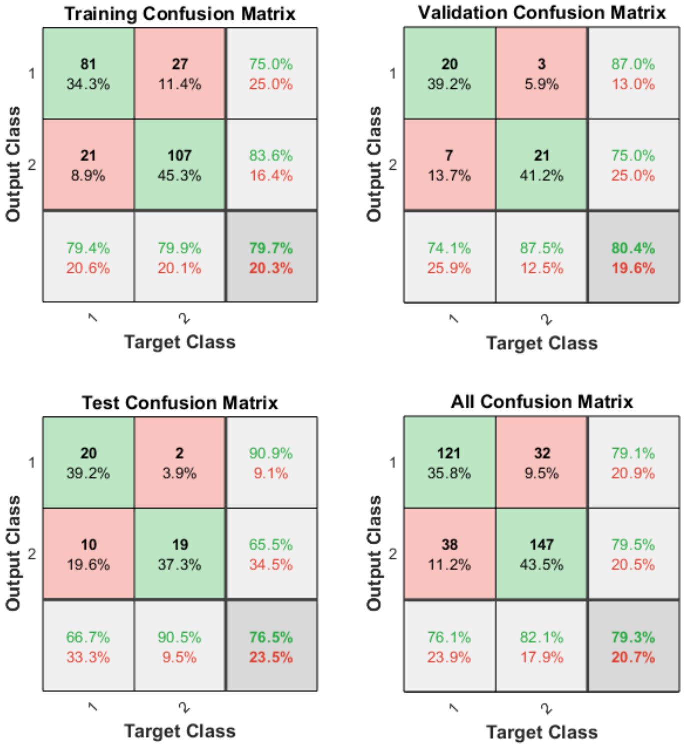

Figure 23: Neural Network Classification Results Using PLE and KS features.
Healthy and tumorous tissue samples were considered for the neural network classifier. Pre-alpha PLE, post-alpha PLE, and post-alpha KS distance were used as features.

The classification accuracy of the ANN model trained on these features was 79.3%. This was the highest correct classification rate of all classifiers studied thus far. To study the contribution that the PLE features have to this classification performance, a second ANN was trained without PLE features. The feature set for this second ANN included the LAC, MSC-Low, PLV, Alpha, Beta, and Gamma features and the performance of this second ANN can be seen in the confusion matrix given below in **Figure 24**.

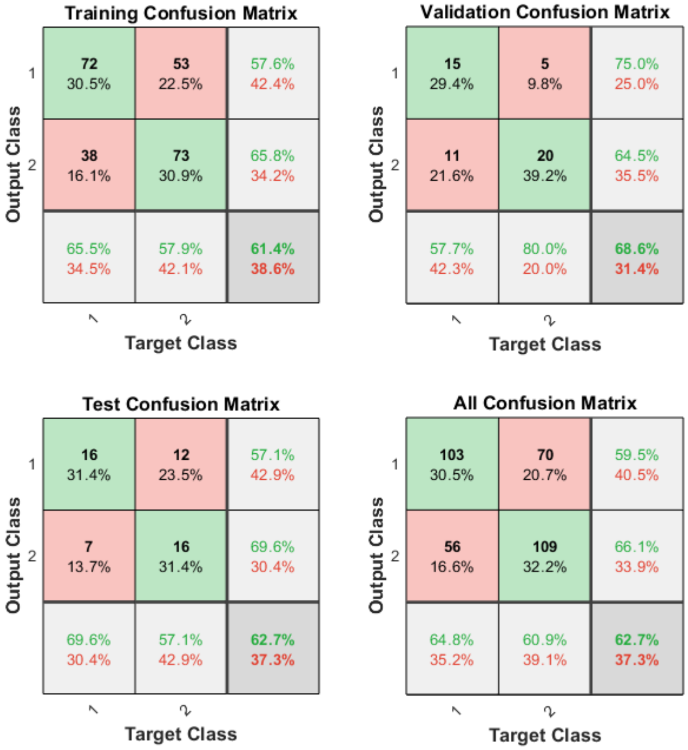

Figure 24: Neural Network Classification Without PLE Features.
These results present the classification performance of an ANN trained using only the LAC, PLV, MSC-Low, Alpha, Beta, and Gamma features.

The classification accuracy of the ANN trained without PLE features was 62.7%. The loss of the PLE features represent a 16.6% decrease in classification accuracy. Considering all classifiers trained thus far, ANNs performed best with 79.3% accuracy while the SVMs and discriminant classifiers remained below 73%. A table of all classifier performances is summarized below in Table 4.

Table 4: LDA, QDA, SVM, and ANN best correct classification rates.

Classifier	**Correct Classification Rate**
LDA	71.3%
QDA	72.8%
SVM	73.0%
ANN	79.3%

5. Discussion

5.1 Summary of Key Findings

I. There are significant differences between tumorous and healthy tissue in pre-alpha PLE, post-alpha PLE, LAC, MSC-Low, PLV, Alpha, Beta, and Gamma features.

II. Classification performance achieved with pre-alpha PLE and post-alpha PLE features alone was 71.3% using a LDA, 72.8% using a QDA classifier, and 73.0% using an SVM. The classification performance of an ANN with LAC, MSC-Low, PLV, Alpha, Beta, and Gamma features was 62.7%; with the addition of the pre-alpha PLE and post-alpha PLE the performance increased to 79.3%. Of all the features explored, the PLE features contribute the most useful information for the classification of tumorous tissue.

III. The LS method of estimating PLE, while theoretically containing more systematic error than the MLE method, produces larger differences between the healthy and tumorous tissue PLE distributions and is more useful as a feature for classification than the MLE PLE.

IV. There is evidence to suggest that the ECoG PSD measured from human subjects with intracranial glioma is well-fit by a power law. The MLE method produces a better power-law fit to the PSD than the LS method.

5.2 Pre-processing Methods

The temporal filters applied to the ECoG data in this work are conservative with respect to how much “good quality” data is being passed into further processing steps. The notch filters have a 10Hz bandwidth, and while these filters do a good job of completely removing the effect of power line interference at 50Hz (and its harmonics) from the data, there is some amount of good data that is being attenuated in that notch bandwidth. Further experimentation could be done to optimize the performance of the notch filters such that a minimal amount of good quality data gets attenuated with the 50Hz components and its aliases. This notch filter improvement may allow for more data points in the post-alpha PLE estimate and this might result in a better fit of the PLE to the measured PSD. With respect to the high-pass filter implemented with a 1Hz cut-off frequency, removal of this filter or optimization of the cut-off frequency may result in more data points being included in the estimate of the pre-alpha PLE, which may reduce the KS test result in the pre-alpha band (increase the goodness-of-fit).

Regarding spatial filters, the application of the CAR filter was experimented with and observationally found to result in cleaner ECoG datasets, the filter having removed components of the data that seemed highly similar. The application of alternative spatial filters was not experimented with. One such alternative filter is the Laplacian spatial filter, which has been applied in sensorimotor rhythm studies and can provide higher or lower resolution spatial filtering of the ECoG data [15]. For the purpose of identifying tumorous tissue, application of a spatial filter with a higher resolution than the CAR may preserve more channel-unique information across a dataset.

5.3 The Power Law Exponent

The CGSA method was implemented with the goal of reducing harmonic peaks throughout the PSD, thus reducing the potential for PLE estimation bias. It was observed in the CGSA-processed PSDs that the harmonic peak reduction effect was minimal and that the CGSA step appeared to smooth out the frequency response. It was also reported by He et al. that, following the implementation of their CGSA, the remaining PSD still contained an unwanted “shoulder” [26]. While the theory of CGSA (see section 3.4.1.1) suggests that the cross power spectral densities of two different times series, each measuring the same data but with different sampling rates, should preserve the scale-free or power law activity more than it should harmonic oscillatory activity, the implementation of the two sampling strategies could have a large effect on the degree to which harmonic and non-harmonic activity is represented in a CSGA output PSD. The sampling strategy chosen in this work was modelled from Yamamoto and Hughson [57]. Yamamoto and Hughson chose to split their time series into epochs, choosing one epoch set as the original set and then replicating every other epoch within the first half of the original set to create a second epoch set equal in length to the first. The method that was implemented in the work presented here also avoids using a coarser sampling rate by creating two different epoch series. While the PSD estimates created with these epoch shuffling methods do reduce the magnitude of harmonic peaks, further reduction is necessary. Specifically, it is expected that there is a large amount of improvement to be done on the coarse sampling method in CGSA. Improved CGSA methods exist in literature [67] but have not been applied in this work. Alternative methods of harmonic activity reduction exist, for example Independent Component Analysis [17], but have not been explored in this work.

The LS method of estimating the PLE produced worse power law fits than the MLE method did for the post-alpha band although the MLE method produced worse power law fits in the pre-alpha band. The pre-alpha band contained noticeably more harmonic peaks than the post-alpha band, with an important note that there were less spectral samples in the pre-alpha band. In the pre-alpha band the initial few spectral power samples likely biased the MLE to produce a PLE estimate. Since MLEs are only guaranteed to be unbiased in the asymptotic limit of large sample size [56], it is likely that the MLE estimator did not have enough samples in its bandwidth to resolve the biasing effect of harmonic perturbations with the available samples. Further study should be completed on the relationship between window size for the CGSA epochs and goodness-of-fit of the power law distribution to the measured pre-alpha PSD. As the CSGA epoch window size becomes larger, the number of points in the lower frequencies, and thus the pre-alpha band, will increase and subsequently bias in the KS result will be reduced. In **Figure 9** the MLE estimate of the PLE is larger than the LS estimate. While the MLE estimated power law distribution appears to be less distant from the sampled PSD through the first harmonic peak, it becomes more distant through the rest of the spectral range than the LS estimated power law PSD becomes. With larger sample size it is likely that the MLE estimate would improve, although further study would be necessary to determine whether large harmonic peaks bias the MLE estimator enough that its estimate would not produce a better power law fit than the LS method.

Figure 11 illustrates the visual differences between the distributions of the LS PLE and MLE PLE. While for the LS methods the PLE distributions appear to have similar variances, the means of the tumorous, peritumoral, and healthy tissue distributions appear slightly but noticeably different. The MLE PLE distributions appear to have less normality and no noticeable difference between mean values. In the MLE pre-alpha PLE distributions the variances are all distinguishably smaller than the other distributions. This is likely due to biasing occurring in the pre-alpha band due to the PSD deviating proportionally further from a power law distribution (visual presentation of a straight line in the log-log PSD) than in the post-alpha band. Further work should be done to study the MLE pre-alpha distribution specifically and its relationship to the number of samples in the CGSA epochs and the cut-off frequency of the high-pass temporal filter. For the purpose of the inclusion of the PLE as a feature for classifying tumorous tissue, the LS PLE method appears to be the better method to use for producing PLE estimates due to the larger significant differences between healthy and tumorous tissue.

Larger significant differences were found between healthy and tumorous tissue with the LS method of PLE estimation than for the MLE method. Specifically, for the pre-alpha band PLE of tumorous tissue is higher than peritumoral PLE which is higher than healthy PLE. This is the opposite case for post-alpha PLE and healthy tissue has the highest PLE, peritumoral tissue the second highest, and tumorous tissue has the lowest. The PLE distributions placed the peritumoral tissue somewhere between the healthy and tumorous tissue distributions, suggesting that the PLE has an ability to measure the degree of influence from an intracranial tumor. A visual presentation of the relationship between tissue type and PLE for a single example subject is shown in **Figure 14**, for which the differences in PLE between these tissue types is immediately apparent. In **Figure 16** it is distinguishable that most subjects follow the same tissue PLE pattern as the subject presented in **Figure 14**. This is reassuring, as it implies that most subjects are well represented by the tissue type and PLE relationship in **Figure 14**.

Figure 13 presents the distributions of pre-alpha LS PLE and post-alpha LS PLE together on the same axis and for all tissue types. From these collective distributions, observing the differences between healthy and tumorous PLE distributions it is apparent that the pre-alpha and post-alpha PLE of the tumorous tissue have larger variance and are closer together than the pre-alpha and post-alpha PLE of the healthy tissue. The heathy tissue distribution is more clearly bi-modal than the tumorous distribution. This suggests that the tumorous tissue PSD is closer to being structured according to a single PLE instead of two different PLEs, although for the tumorous case the pre- and post- distributions still do not appear to come from the same distribution. Further studies should be completed on the relationship between tissue PLE and behavioural processes within each of the pre- and post- bands. Colombo et al. found that, in the case of studying the degree of wakefulness in patients given anesthesia, the PLE indexed the presence of consciousness [24]. The higher similarity between the pre-and post- distributions for tumorous tissue may be associated with changes in behavioural processes characterized by long range temporal correlations in each of the pre-alpha and post-alpha bands.

5.4 Spectral Amplitudes

It was expected that some of the information contained in the PLE analysis of healthy and tumorous tissue would also represent itself similarly in the spectral amplitude features. If a power law distribution has a steeper or shallower structure, it follows that the ratios of power in different spectral bandwidths would change. While the delta bandwidth is contained in the pre-alpha bandwidth and the gamma bandwidth is contained within the post-alpha bandwidth, the alpha and beta bandwidths (7- 13Hz and 14-30Hz, respectively) are not represented in the pre-alpha or post-alpha bandwidths. This implies that the information within the alpha and beta features will be novel when combined with the PLE features in classification. Coincidentally, but perhaps not independently from the PLE effect (this is yet to be studied), the alpha and beta bands showed the largest significant differences in amplitude between healthy and tumorous tissue. The gamma band amplitude difference between healthy and tumorous tissue was also significant but to a lesser extent than the alpha and beta bands. The delta band difference was not significant although healthy tissue did appear to have a higher mean amplitude than tumorous tissue. For the delta band the absence of a significant difference between healthy and tumorous tissue may be associated with the cause of the lower significant difference in the pre-alpha PLE than the post-alpha PLE. The lowest frequencies appeared to contain the largest harmonic peaks, except the alpha-beta frequencies between the pre-alpha and post-alpha bandwidths which contained a large “knee”. These harmonic peaks, along with an absence of as many spectral samples as in the post-alpha band, are most likely the cause of the poor-fit pre-alpha PLE and also the lack of difference between the delta-band healthy tissue and tumorous tissue amplitudes.

These results, without further improvement of low-frequency representation and for the purpose of classifying tumorous tissue, support placing a higher importance in features generated using higher frequencies, such as the alpha, beta, and gamma band amplitudes as well as the post-alpha PLE. Overall, the spectral features do not identify as much difference between healthy and tumorous distributions as the LS PLE features do. The existence of difference between healthy and tumorous distributions in the spectral amplitude features is important due to the relevance of spectral amplitude features in literature [12].

5.5 Functional Connectivity Features

While a significant difference was found between healthy and tumorous distributions for the PLV, MSC-Low, and LAC, a significant difference was not found for the PLI or the MSC-High features. More phase locking to adjacent channels was found in the 30-40Hz bandwidth in tumorous tissue than in healthy tissue. More magnitude coherence to adjacent channels was found in tumorous channels than in healthy channels. More amplitude correlation with adjacent channels was found in tumorous channels than in healthy channels. With respect to both amplitude and phase, there was more functional connectivity to adjacent channels identified for tumorous tissue than healthy tissue. This suggests that functional connectivity is an important concept to consider for the classification of tumorous tissue.

The PLV feature identified significant difference between tumorous and healthy channels within the 30-40Hz bandwidth. Other bandwidths were experimented with and while no significant differences were found within the 0-8Hz or 8-12Hz bandwidths, significant differences were found within the 14-30Hz and 30-100Hz bandwidths. The 30-40Hz bandwidth presented in this work is the bandwidth for which the largest significant difference between tissue types was found. The PLV algorithm applied in this work only considered the phase locking between channels within one bandwidth, and not phase locking between different bandwidths. The phase locking between lower and higher bandwidths had been studied in literature and modulatory relationships discovered between these bandwidth ranges [26,32]. For this reason, future studies should focus on looking at the PLV not only within specific bandwidths but also between different bandwidths.

The PLI feature did not identify significant differences between healthy and tumorous tissue. However, the tumorous distribution contained more samples in higher PLI bins. The variance of the tumorous distribution was smaller than of the healthy distributions however, so no significance was found between the mean values of the two tissue distributions. It was expected that the PLI would produce similar results to the PLV feature, as both use the instantaneous phase from the Hilbert transform and both average phases differences across temporal samples. This was not the case however and may in part be due to the bandwidths of study being different between the two features. A band-limited PLI may reveal significant difference between tissue types but band-limiting methods were not applied for the PLI in this work.

Both the MSC-Low and LAC features identified tumorous tissue to have more amplitude coherence and correlation to adjacent electrode channels, respectively, than healthy tissue. This was not the case for the The LAC feature studied full bandwidth correlation however, while the MSC-Low studied coherence within the 0-4Hz bandwidth. The healthy and tumorous tissue MSC-Low distributions appear highly similar to the LAC distributions. This high degree of similarity implies that the significant difference found between tissue types for the LAC feature may be coming from the lower frequency bandwidth 0-4Hz.

The spatial selection of electrodes was the same for each of the functional connectivity features studied within this work. An adjacent electrode selection scheme was chosen for these features in order to represent a short ranged functional connectivity. A longer ranged functional connectivity scheme can be created by including more distant electrodes in the calculations for the connectivity features. The only alternative scheme studied for this work was one in which all electrodes were included in the functional connectivity feature calculations for each electrode, the final feature value for the electrode achieved by averaging over all electrode comparisons. This alternative did not result in any significant differences between tissue types for any of the features, so it was not studied further.

5.6 Tumorous Tissue Classification

The two discrimination analysis methods used for classification performed similarly when applied to the pre-alpha and post-alpha LS PLE feature space. In this feature space, the healthy and tumorous distributions appear to be different, with the healthy distribution appearing more normally distributed than the tumorous distribution, which appears more elliptical. There are, however, a large number of samples in the tumorous feature space that occupy the same space as the center of the healthy distribution. Therefor, classification of tumorous tissue is expected to be a difficult task using only these two features. In this feature space the LDA achieved a correct classification rate of 71.3% and the QDA 72.8%. These classification rates are not satisfactory for the purpose of proving the utility of the PLE features alone in classification. A support vector machine (SVM) method of classification was explored to improve the tumorous tissue classification performance. This SVM was applied to the full set of features that had identified significant differences between healthy and tumorous tissue (pre-alpha PLE, post-alpha PLE, PLV, MSC-Low, LAC, alpha, beta, gamma). The performance of the SVM was poorer than expected at 73.0%. While the PLE features had been used to achieve a similar performance, the additional functional connectivity and spectral amplitude features did not contribute additional discriminative power. An artificial neural network (ANN) was then trained on the same set of features used with the SVM. The performance with these features was 79.3%. An ANN was subsequently trained only on the PLV, MSC-Low, LAC, alpha, beta, and gamma features. The performance of this second ANN was 62.7%. This reduced performance represents a very large loss of useful information with the exclusion of the PLE features in the case of ANN classification. The performance of classifiers reported in literature were all higher than the best performances achieved in this work. One explanation for this is the limited number of subjects presented in studies reporting very high classification accuracy; this limitation may result in biased performance. Another explanation for this is the processes used for inclusion and exclusion of data in studies reported in literature. These processes are often not described in thorough detail. As a result, it is difficult to compare inclusion and exclusion criteria of different studies and to ascertain whether or not these criteria are greatly affecting classification performance. Lastly, the work presented in this thesis included similar but not identical filtering methodology to the studies presented in literature. The feature selection and ANN architecture reported by Boussen et al. [25] compare directly to the work presented in this thesis. Boussen et al reported an 87% classification accuracy of tumorous tissue while this work achieved 79.3% with the addition of PLE features, while using the same ANN architecture. The most likely cause of the difference in these classification performances is theorized here to be the different datasets used for the two studies.

In summary, both PLE features contribute more to a higher classification performance than the combination of all spectral amplitude and functional connectivity features explored in this work. All features, including the PLE, have room left in their algorithms for relatively obvious improvements to be made.

6. Conclusions

The objectives of this study were as follows:

1. Evaluate the utility of the PLE in the classification of tumorous tissue using ECoG data from awake and resting subjects.
2. Evaluate the utility of functional connectivity features and spectral amplitude features in the classification of tumorous tissue using ECoG data from awake and resting subjects.
3. Classify tumorous tissue using PLE, functional connectivity, and spectral amplitude features and determine which features are more important for achieving high classification performance.

Objective 1 was completed. The PLE was used to achieve a 72.8% correct classification rate for tumorous tissue. The PLE is a valuable feature for use in the classification of tumorous tissue. Objective 2 was completed. The PLV, MSC-Low, LAC, alpha, beta, gamma features do not contribute a large amount of useful information for the classification of tumorous tissue. This was determined by the 62.7% classification performance of the ANN using this feature set. Additional study is necessary to prove that alternative formulations of the functional connectivity algorithms are not capable of achieving a higher classification rate with the dataset studied in this work. Objective 3 was completed. Classification performance using the pre-alpha PLE, post-alpha PLE, PLV, MSC-Low, LAC, alpha, beta, and gamma features is at best ~80% with the ANN model used in this work. The 62.7% correct classification rate with an ANN and with the above features but without the PLE features, demonstrates that the PLE features are more important than the functional connectivity features and spectral amplitude features for the classification of tumorous tissue.

The primary novel contribution in this work is the demonstration of tumorous tissue classification efficacy using PLE features. Furthermore, this work contains an original derivation of the MLE PLE for application with power spectral densities specifically. Additionally, this work shows for the first time that the LS PLE method is a better method than the MLE PLE method for tumorous tissue classification. Lastly, this work compares the LS PLE feature utility to that of spectral amplitude and functional connectivity features for the first time.

7. Future Directions

While the PLE methods and results contained in this work have been analyzed and discussed to some depth, the functional connectivity and spectral amplitude features were not analyzed and discussed to an equivalent depth. The features beyond the PLE features were intended to connect and compare the PLE research to existing literature completed with the other features. The functional connectivity and spectral features, therefor, deserve additional attention in further studies with this dataset, and improvements to those feature methods may result in further understanding of the dependence between features and which ones are the best features to include in further studies that include more rigorous classification experimentation. It should be noted here that all functional connectivity methods used the same spatial selection scheme for electrodes, including comparisons only with an electrodes' immediate neighbours. This spatial selection should be studied further.

The pre-alpha PLE results achieved in this work demonstrate the need for inclusion of additional spectral samples within the pre-alpha PLE bandwidth. This can be achieved with larger CGSA epoch windowing and should be applied in further studies. An additional factor that affected the pre-alpha PLE results was the harmonic peaking activity within the pre-alpha bandwidth. These peaks can be reduced further and more non-harmonic activity preserved if the CGSA method can be improved such that it attenuates harmonic activity to a greater extent. Regarding the averaging performed in the construction of a single PSD estimate of the ECoG data, Heathcote et al. found that averaging caused a bias towards power law fitting and that an exponential scaling should be evaluated alongside power law scaling in cases that could be affected by this averaging bias [62]. This effect should be evaluated more thoroughly in further studies.

Regarding the temporal and spatial filtering applied in this work, alternative pre-processing methods such as Laplacian filters and tuned temporal filters were not explored. Improvements in these pre-processing methods may reveal larger differences between healthy and tumorous distribution for studied feature spaces.

Regarding the study of intracranial tissue, this work focused on studying the classification of tumorous tissue and included only the ECoG electrodes that overlay healthy or tumorous tissue. A third tissue class was included in this dataset: peritumoral tissue. Peritumoral tissue classification is important because it has been suggested that greater surgical resection of the lesion as well as the epileptogenic zone associated with it results in improved overall survival, progression-free survival, and superior quality of life [4]. While the definition of this tissue class is clear, *i.e.* tissue lying within a two-centimeter margin from the tumorous tissue borders, this type of tissue has not been investigated in literature as much as healthy and tumorous tissue are [18,25,40,41,42,43]. This tissue was explored using PLE features but was not explored with the other features. The PLE distributions placed the peritumoral tissue somewhere between the healthy and tumorous tissue distributions, suggesting that the PLE has an ability to measure the degree of influence from an intracranial tumor. This is a highly interesting discovery that should be further explored in additional experiments or by improving spatial filtering methods such that more uniqueness within channels.

8. References

[1] A. Omuro and L. M. DeAngelis, "Glioblastoma and other malignant gliomas: A clinical review," *JAMA - Journal of the American Medical Association,* vol. 310, p. 1842–1850, 2013.

[2] J. Pallud, E. Audureau, M. Blonski, N. Sanai, L. Bauchet, D. Fontaine, E. Mandonnet, E. Dezamis, D. Psimaras, J. Guyotat, P. Peruzzi, P. Page, B. Gal, E. Párraga, M. H. Baron, M. Vlaicu, R. Guillevin, B. De'aux, H. Duffau, L. Taillandier, L. Capelle and G. Huberfeld, "Epileptic seizures in diffuse low-grade gliomas in adults," *Brain,* vol. 137, p. 449–462, 2014.

[3] A. Kuruvilla and R. Flink, "Intraoperative electrocorticography in epilepsy surgery: Useful or not?," *Seizure,* vol. 12, p. 577–584, 2003.

[4] S. L. Hervey-Jumper and M. S. Berger, "Maximizing safe resection of low- and high-grade glioma," *Journal of Neuro-Oncology,* vol. 130, p. 269–282, 2016.

[5] J. Engel, "Surgery for Seizures," *New England Journal of Medicine,* vol. 334, p. 647–653, 1996.

[6] C. Im and J.-M. Seo, "A Review of Electrodes for the Electrical Brain Signal Recording," *Biomedical Engineering Letters,* vol. 6, pp. 104-112, 2016.

[7] B. Burle, C. R. L. C. Laure Spieser, T. Hasbroucq and F. Vidal, "Spatial and temporal resolutions of EEG: Is it really black and white? A scalp current density view," *International Journal of Psychophsiology,* vol. 97, pp. 210-220, 2015.

[8] N. Hill, D. Gupta, P. Brunner, A. Gunduz, M. A. Adamo, A. Ritaccio and G. Schalk, "Recording Human Electrocorticographic (ECoG) Signals for Neuroscientific Research and Real-time Functional Cortical Mapping," *Journal of Visualized Experiments,* vol. 64, pp. 1-5, 2012.

[9] A. Dubey and S. Ray, "Cortical electrocorticogram (Ecog) is a local signal," *Journal of Neuroscience,* vol. 39, p. 4299–4311, 2019.

[10] A. Dubey and S. Ray, "Spatial spread of local field potential is band-pass in the primary visual cortex," *Journal of Neurophysiology,* vol. 116, p. 1986–1999, 2016.

[11] N. E. Crone, A. Sinai and A. Korzeniewska, "Chapter 19 High-frequency gamma oscillations and human brain mapping with electrocorticography," *Progress in Brain Research,* vol. 159, p. 275–295, 2006.

[12] Christa Neuper and Wolfgang Klimesch, "Event-Related Dynamics of Brain Oscillations," *Methods in cell science : an official journal of the Society for In Vitro Biology,* vol. 22, p. 25, 2000.

[13] S. H.-F. Syam, H. Lakany, R. Ahmad and B. A. Conway, "Comparing Common Average Referencing to Laplacian Referencing in Detecting Imagination and Intention of Movement for Brain Computer Interface," *MATEC Web of Conferences,* vol. 140, pp. 1-7, 2017.

[14] Y. Liu, W. G. Coon, A. d. Pesters, P. Brunner and G. Shalk, "The effects of spatial filtering and artifacts on electrocorticographic signals," *Journal of Neural Engineering,* vol. 12, no. 5, 2015.

[15] D. Mcfarland, L. McCane, S. David and J. Wolpaw, "Spatial filter selection for EEG-based communication," *Electroencephalography and clinical Neurophysiology,* vol. 103, pp. 386-394, 1997.

[16] T. Ball, M. Kern, I. Mutschler, A. Aertsen and A. Schulze-Bonhage, "Signal quality of simultaneously recorded invasive and non-invasive EEG," *NeuroImage,* vol. 46, pp. 708-716, 2009.

[17] J. Iriarte, E. Urreestarazu, M. Valencia, M. Alegre, A. Malanda, C. Viteri and J. Artieda, "Independent Component Analysis as a Tool to Eliminate Artifacts in EEG: A Quantitative Study," *Journal of Clinical Neurophysiology,* vol. 20, no. 4, pp. 249-257, 2003.

[18] M. Sharanreddy and P. K. Kulkarni, "Automated EEG signal analysis for identification of epilepsy seizures and brain tumour," *Journal of Medical Engineering and Technology,* vol. 37, p. 511–519, 2013.

[19] K. J. Friston, "Functional and effective connectivity in neuroimaging: A synthesis," *Human Brain Mapping,* vol. 2, p. 56–78, 1994.

[20] G. Nolte, O. Bai, L. Wheaton, Z. Meri, S. Vorbach and M. Hallett, "Identifying true brain interaction from EEG data using," *Clinical Neurophysiology* , vol. 115, pp. 2292-2307, 2004.

[21] M. G. Rosenblum, A. S. Pikovsky and a. J. Kurths, "Phase Synchronization of Chaotic Oscillators," *Physical Review Letters,* vol. 76, no. 11, pp. 1804-1807, 1996.

[22] L. Astolfi, F. Cincotti, D. Mattia, S. Salinari, C. Babiloni, A. Basilisco, P. M. Rossini, L. Ding, Y. Ni, B. He, M. G. Marciani and F. Babiloni, "Estimation of the effective and functional human cortical connectivity with structural equation modeling and directed transfer function applied to high-resolution EEG," *Magnetic Resonance Imaging,* vol. 22, p. 1457–1470, 2004.

[23] E. Niedermeyer, D. L. Schomer and F. H. L. d. SIlve, Niedermeyer’s Electroencephalography: Basic Principles, Clinical Applications, and Related Fields, 2011, p. 935–948.

[24] M. A. Colombo, M. Napolitani, M. Boly, O. Gosseries, S. Casarotto, M. Rosanova, J. F. Brichant, P. Boveroux, S. Rex, S. Laureys, M. Massimini, A. Chieregato and S. Sarasso, "The spectral exponent of the resting EEG indexes the presence of consciousness during unresponsiveness induced by propofol, xenon, and ketamine," *NeuroImage,* vol. 189, p. 631–644, 2019.

[25] S. Boussen, L. Velly, C. Benar, P. Metellus, N. Bruder and A. Trébuchon, "In Vivo Tumour Mapping Using Electrocorticography Alterations During Awake Brain Surgery: A Pilot Study," *Brain Topography,* vol. 29, p. 766–782, 2016.

[26] B. J. He, J. M. Zempel, A. Z. Snyder and M. E. Raichle, "The Temporal Structures and Functional Significance of Scale-free Brain Activity," *Neuron*, vol. 66, pp. 353-369, 2010.

[27] W. S. Pritchard, "The brain in fractal time: 1/f-like power spectrum scaling of the human electroencephalogram," *International Journal of Neuroscience,* vol. 66, p. 119–129, 1992.

[28] K. Linkenkaer-Hansen, V. V. Nikouline, J. M. Palva and R. J. Ilmoniemi, "Long-Range Temporal Correlations and Scaling Behavior in Human Brain Oscillations".

[29] S. Vanhatalo, J. M. Palva, M. D. Holmes, J. W. Miller, J. Voipio and K. Kaila, "Infraslow oscillations modulate excitability and interictal epileptic activity in the human cortex during sleep," *Proceedings of the National Academy of Sciences,* vol. 101, no. 14, pp. 5053-5057, 2004.

[30] R. T. Canolty, E. Edwards, S. S. Dalal, M. Soltani, S. S. Nagarajan, H. E. Kirsch, M. S. Berger, N. M. Barbare and R. T. Knight, "High gamma power is phase-locked to theta oscillations in human neocortex," *Science,* vol. 313, p. 1626–1628, 2006.

[31] A. G. Casali, O. Gosseries, M. Rosanova, M. Boly, S. Sarasso, K. R. Casali, S. Casarotto, M. A. Bruno, S. Laureys, G. Tononi and M. Massimini, "A theoretically based index of consciousness independent of sensory processing and behavior," *Science Translational Medicine,* vol. 5, 2013.

[32] Z. Huang, J. Zhang, A. Longtin, G. Dumont, N. W. Duncan, J. Pokorny, P. Qin, R. Dai, F. Ferri, X. Weng and G. Northoff, "Is There a Nonadditive Interaction Between Spontaneous and Evoked Activity? Phase-Dependence and Its Relation to the Temporal Structure of Scale-Free Brain Activity," *Cerebral Cortex,* 2015.

[33] C. Bédard, H. Kröger and A. Destexhe, "Does the 1/f frequency scaling of brain signals reflect self-organized critical states?," *Physical Review Letters,* vol. 97, p. 1–4, 2006.

[34] D. P. Almond and B. Vainas, "The electrical characteristics of random RC networks and the physical origin of 1/f noise," *Journal of Physics Condensed Matter,* vol. 13, 2001.

[35] K. J. Miller, L. B. Sorenson, J. G. Ojemann and M. d. Nijs, "Power-Law Scaling in the Brain Surface Electric Potential," *PLoS Computational Biology,* vol. 5, no. 12, 2009.

[36] S. K. Bandt, J. L. Roland, M. Pahwa, C. D. Hacker, D. T. Bundy, J. D. Breshears, M. Sharma, J. S. Shimony and E. C. Leuthardt, "The impact of high grade glial neoplasms on human cortical electrophysiology," *PLoS ONE,* 2017.

[37] J. Hlinka, M. Palus, M. Vejmelka, D. Mantini and M. Corbetta, "Functional connectivity in resting-state fMRI: Is linear correlation sufficient?," *NeuroImage,* vol. 54, no. 3, pp. 2218-2225, 2011.

[38] C. J. Stam, G. Nolte and A. Daffertshofer, "Phase lag index: Assessment of functional connectivity from multi channel EEG and MEG with diminished bias from common sources," *Human Brain Mapping,* vol. 28, p. 1178–1193, 2007.

[39] J. P. Lachaux, E. Rodriguez, J. Martinerie and F. J. Varela, "Measuring phase synchrony in brain signals," *Human Brain Mapping,* vol. 8, p. 194–208, 1999.

[40] F. N. Karameh and M. A. Dahleh, *Automated classification of EEG signals in brain tumor diagnostics,* vol. 6, 2000, p. 4169–4173.

[41] M. Murugesan and RSukanesh, "Automated detection of brain tumor in EEG signals using artificial neural networks," *ACT 2009 - International Conference on Advances in Computing, Control and Telecommunication Technologies,* p. 284–288, 2009.

[42] M. Murugesan and R. Sukanesh, "Towards Detection of Brain Tumor in Electroencephalogram Signals Using Support Vector Machines," *International Journal of Computer Theory and Engineering,* vol. 1, p. 622–631, 2009.

[43] V. S. Selvam and S. Shenbagadevi, "Brain tumor detection using scalp eeg with modified Wavelet-ICA and multi layer feed forward neural network.," *Conference proceedings : ... Annual International Conference of the IEEE Engineering in Medicine and Biology Society. IEEE Engineering in Medicine and Biology Society. Conference,* vol. 2011, p. 6104–6109, 2011.

[44] J. H. Friedman, "Regularized discriminant analysis," *Journal of the American Statistical Association,* vol. 84, p. 165–175, 1989.

[45] S. Velilla and A. Hernández, "On the consistency properties of linear and quadratic discriminant analyses," *Journal of Multivariate Analysis,* vol. 96, p. 219–236, 2005.

[46] C. Cortes and V. Vapnik, "Support Vector Networks," *Machine Learning,* vol. 20, p. 273–297, 1995.

[47] Marti A. Hearst, "Support vector machines," *IEEE Intelligent Systems: Trends and Controversies,* p. 18–21, 1998.

[48] E. Byvatov, U. Fechner, J. Sadowski and G. Schneider, "Comparison of Support Vector Machine and Artificial Neural Network Systems for Drug/Nondrug Classification," *Journal of Chemical Information and Computer Sciences,* vol. 43, p. 1882–1889, 2003.

[49] G. P. Zhang, "Neural Networks for Classification: A Survey," *IEEE TRANSACTIONS ON SYSTEMS, MAN, AND CYBERNETICS—PART C: APPLICATIONS AND REVIEWS,* vol. 30, no. 4, pp. 451-462, 2000.

[50] R. P. Lippmann, "An Introduction to Computing with Neural Nets," *IEEE ASSP Magazine* , vol. 4, no. 2, pp. 4-22, 1987.

[51] D. Ghinda, N. Zhang, J. Lu, C. J. Yao, S. Yuan and J. S. Wu, "Contribution of combined intraoperative electrophysiological investigation with 3-T intraoperative MRI for awake cerebral glioma surgery: Comprehensive review of the clinical implications and radiological outcomes," *Neurosurgical Focus,* vol. 40, p. 1–11, 2016.

[52] M. Osswald, E. Jung, F. Sahm, G. Solecki, V. Venkataramani, J. Blaes, S. Weil, H. Horstmann, B. Wiestler, M. Syed, L. Huang, M. Ratliff, K. K. Jazi, F. T. Kurz, T. Schmenger, D. Lemke and W. W. &. F. Winkler, *Brain tumour cells interconnect to a functional and resistant network,* 2015.

[53] M. Osswald, G. Solecki, W. Wick and F. Winkler, "A malignant cellular network in gliomas: Potential clinical implications," *Neuro-Oncology,* vol. 18, p. 479–485, 2016.

[54] B. M. Ellingson, P. Y. Wen and T. F. Cloughesy, "Modified Criteria for Radiographic Response Assessment in Glioblastoma Clinical Trials," *Neurotherapeutics,* vol. 14, p. 307–320, 2017.

[55] D. Englot, M. Berger, E. C. NM Barbaro and S. Francisco, "Predictors of seizure freedom after resectionof supratentorial low-grade gliomas," *Journal of Neurosurgery,* vol. 115, pp. 240-244, 2011.

[56] A. Clauset, C. R. Shalizi and M. E. J. Newman, "Power-Law Distributions in Empirical Data," *SIAM Review,* 2009.

[57] Y. Yamamoto and R. L. Hughson, "Coarse-graining spectral analysis: for studying heart rate variability new method".

[58] B. B. Mandelbrot and J. W. V. Ness, "Fractional Brownian Motions, Fractional Noises and Applications," *SIAM Review,* vol. 10, no. 4, pp. 422-437, 1968.

[59] Y. Yamamoto and R. L. Hughson, "Coarse-graining spectral analysis: new method for studying heart rate variability," *Journal of Applied Physiology,* vol. 71, no. 3, pp. 1143-1150, 1991.

[60] K. J. Miller, L. B. Sorensen, J. G. Ojemann and M. Den Nijs, "Power-law scaling in the brain surface electric potential," *PLoS Computational Biology,* vol. 5, 2009.

[61] W. H. Press, S. A. Teukolsky, W. T. Vetterling and B. P. Flannery, Numerical Recipes in C, vol. 76, 1992, p. 19–21.

[62] A. Heathcote, S. Brown and D. J. K. Mewhort, "The power law repealed: The case for an exponential law of practice," *Psychonomic Bulletin and Review,* vol. 7, p. 185–207, 2000.

[63] B. Efron and R. J. Tibshirani, *An Introduction to the Bootstrap,* 1993, p. 68–74.

[64] R. A. Fisher, Stastical Methods for Research Workers, Oliver and Boyd, 1950.

[65] T. Gasser, P. Bächer and J. Möcks, "Transformations towards the normal distribution of broad band spectral parameters of the EEG," *Electroencephalography and Clinical Neurophysiology,* vol. 53, p. 119–124, 1982.

[66] C. M. Bishop, "Neural Networks for Pattern Recognition," *Advances in Computers,* vol. 37, p. 119–166, 1995.

[67] H. Wen and Z. Liu, "Separating Fractal and Oscillatory Components in the Power Spectrum of Neurophysiological Signal," *Brain Topography,* vol. 29, pp. 13-26, 2016.

[68] D. Hush, "Classification with Neural Networks: A Performance Analysis," in *IEEE 1989 International Conference on Systems Engineering,* Fairborn, OH, USA, 1989.

[69] J. Naranjo, "New views made easy – Visualizing ECoG grids & connectivity matrices via Analyzer 2’s MATLAB® transformation," Brain Products, 21 April 2017. [Online]. Available: https://pressrelease.brainproducts.com/matlab-transform/. [Accessed 15 01 2021].